Brain Stimulation 19 (2026) 103016

Contents lists available at ScienceDirect

Brain Stimulation

journal homepage: www.journals.elsevier.com/brain-stimulation

TI-Toolbox: An open-source software for temporal interference stimulation research

Ido Haber [a,b], Aksel Jackson [c,d], Axel Thielscher [e,f], Aviad Hai [b,g,h], Giulio Tononi [a,*]

[a] Department of Psychiatry, University of Wisconsin-Madison, Madison, WI, USA
[b] Department of Biomedical Engineering, University of Wisconsin-Madison, Madison, WI, USA
[c] Department of Computer Science, University of Wisconsin-Madison, Madison, WI, USA
[d] Department of Philosophy, University of Wisconsin-Madison, Madison, WI, USA
[e] Danish Research Centre for Magnetic Resonance, Department of Radiology and Nuclear Medicine, Copenhagen University Hospital Amager and Hvidovre, Hvidovre, Denmark
[f] Technical University of Denmark, Section for Magnetic Resonance, Department of Health Technology, Kongens Lyngby, Denmark
[g] Wisconsin Institute for Translational Neuroengineering, University of Wisconsin-Madison, Madison, WI, USA
[h] Department of Electrical and Computer Engineering, University of Wisconsin–Madison, Madison, WI, USA

ARTICLE INFO

Keywords:
Temporal interference
Brain stimulation
Neuroimaging
Computational modeling
SimNIBS
Open-source software

ABSTRACT

Background: Temporal interference (TI) stimulation is a novel non-invasive brain stimulation approach that promises selective targeting of deep brain structures while minimizing off-target cortical stimulation. Despite a growing interest in TI applications, there is a need for integrated computational tools that seamlessly connect neuroimaging data preprocessing through montage optimization, field simulation, and analysis within a unified framework designed for translational and clinical research.

Methods: We developed TI-Toolbox, an open-source software platform that integrates established neuroimaging tools (dcm2niix, SimNIBS, FreeSurfer) with specialized algorithms for TI research. The platform provides end-to-end workflows encompassing structural MRI preprocessing, volume conduction modeling, montage optimization, electric field simulation, and region-of-interest analysis. Both graphical user interface and command-line interface implementations ensure accessibility across user expertise levels. The platform employs containerized deployment via Docker to ensure reproducibility and cross-platform compatibility.

Results: TI-Toolbox successfully automates the complete TI research pipeline, from DICOM conversion through final field analysis. The platform demonstrates robust performance across operating systems and provides standardized workflows that enhance reproducibility. Furthermore, our case studies support the validity of our HD-EEG mapping approach for montage standardization and the need for individualized modeling for exposure assessment.

Conclusions: TI-Toolbox addresses critical infrastructure gaps in TI research by providing researchers with a unified, validated platform that reduces technical barriers and accelerates translational research in non-invasive deep brain stimulation.

1. Introduction

Temporal interference (TI) stimulation has emerged as a promising technique for non-invasive neuromodulation, offering better stimulation focality when targeting deep brain structures compared to traditional transcranial electrical stimulation (tES) modalities [1]. Unlike conventional tES methods that predominantly affect superficial cortical regions, TI employs kilohertz-frequency carriers through multiple electrode pairs with a physiologically relevant offset frequency to create focal stimulation at depth (e.g. 2.0 kHz and 2.01 kHz) (Fig. 1) [2].

While early hypotheses proposed that neurons would only respond to the beat frequency due to their intrinsic low pass filtering, recent evidence suggests that neurons are affected by kilohertz-frequency stimulation through direct membrane polarization, with stimulation thresholds increasing with frequency [3–5]. Though there is not yet an established mechanistic explanation, the neural response to TI likely

* Corresponding author. Dept. of Psychiatry University of Wisconsin-Madison 6001 Research Park Blvd Madison, WI, 53719, USA.
E-mail address: gtononi@wisc.edu (G. Tononi).

https://doi.org/10.1016/j.brs.2025.103016
Received 9 October 2025; Received in revised form 22 December 2025; Accepted 22 December 2025
Available online 2 January 2026

involves a non-linear process [6,7]. Recent reviews provide comprehensive listings of emerging TI studies [8–10] with preclinical studies demonstrating successful modulation of hippocampal activity and motor cortex functions [11,12] while human studies report effects on improvement of working memory, reduction of epileptic biomarkers, and enhancement of slow wave activity during sleep [5,13,14].

While researchers are actively working to decipher the neural mechanisms of TI at the microscopic level, modulation of the central nervous system critically depends on the electric field strength and likely its orientation relative to the neural tissue in line with more traditional tES interventions [15,16]. Therefore, knowing the electric field exposure is essential for planning rigorous clinical studies. Some studies take advantage of depth electrodes for cohorts that have surgical implants, which allows field distribution to be assessed directly and tuned towards the desired target [5,17]. However, in most human studies, participants do not have implanted electrodes, making it impossible to directly measure the brain's exposure to TI stimulation.

To address this challenge, in-silico simulations offer a powerful, non-invasive solution which enables researchers to estimate field exposure across the entire head with high spatial resolution, under controlled and reproducible conditions [18]. These simulations are well-suited for conducting experimental manipulations, optimizing stimulation protocols, and minimizing possible risk to participants [19,20]. Several TI tools exist, including commercial solutions [21–24] and open-source alternatives [25–27]. In practice, however, existing solutions remain fragmented, often requiring researchers to assemble custom pipelines, or proving inaccessible due to steep learning curves or high licensing costs [8]. This fragmentation poses significant challenges for establishing standardized workflows and hinders the broader clinical application of in-silico TI modeling.

Here, we introduce TI-Toolbox, an open-source platform that offers a comprehensive, integrated, end-to-end solution designed to tackle the key challenges in clinical TI research. The platform combines established neuroimaging tools within a unified framework specifically designed for TI applications, offering automated workflows from raw magnetic resonance imaging (MRI) data through optimized stimulation protocols and detailed field analysis (Fig. 2). TI-Toolbox aims to promote access to advanced TI modeling by unifying preprocessing, optimization, simulation, analysis and visualization within a single framework that promotes computational ease of use, reproducibility, and methodological standardization across the research community.

Using TI-Toolbox, we sought to answer multiple concerns that the field has been debating: (Q1) Does mapping optimal montages obtained through unconstrained genetic optimization onto standard high-density EEG (HD-EEG) nets alter electric field characteristics [28,29]? (Q2) Does a personalized model for montage optimization provide a meaningful advantage over using a montage derived from a generalized model [30]? (Q3) Can demographic or anatomical factors explain inter-individual variability in TI exposure? To answer these questions, we evaluated three ROIs: the left insula, the right hippocampus, and a spherical ROI centered at MNI coordinates (36.10, 14.14, 0.33) with radius 5 mm, while assessing the intensity, direction, and focality of the maximal modulation vector field. Understanding the appropriateness of electrode placement discretization via EEG nets and the usage of generic head models for montage optimization has the potential to improve clinical trial design and support reproducibility.

2. Methods

2.1. Overview

The TI-Toolbox is organized into four main components: preprocessing, optimization, simulation, and analysis (Fig. 2). The modules are designed to operate in a linear sequence, with standardized data structures and outputs enabling reproducibility across stages. The preprocessing module generates subject-specific head models from raw MRI data via automated DICOM conversion, surface reconstruction, and finite element meshing. The optimization module determines effective electrode montages fitted to the subject anatomy and a stimulation objective, supporting both genetic and exhaustive algorithms. The simulation module computes subject-specific electric fields and TI envelopes, with support for directional field components, multi-polar TI, and customizable electrode montages. The analysis module extracts region-wise metrics and generates visualizations through either surface

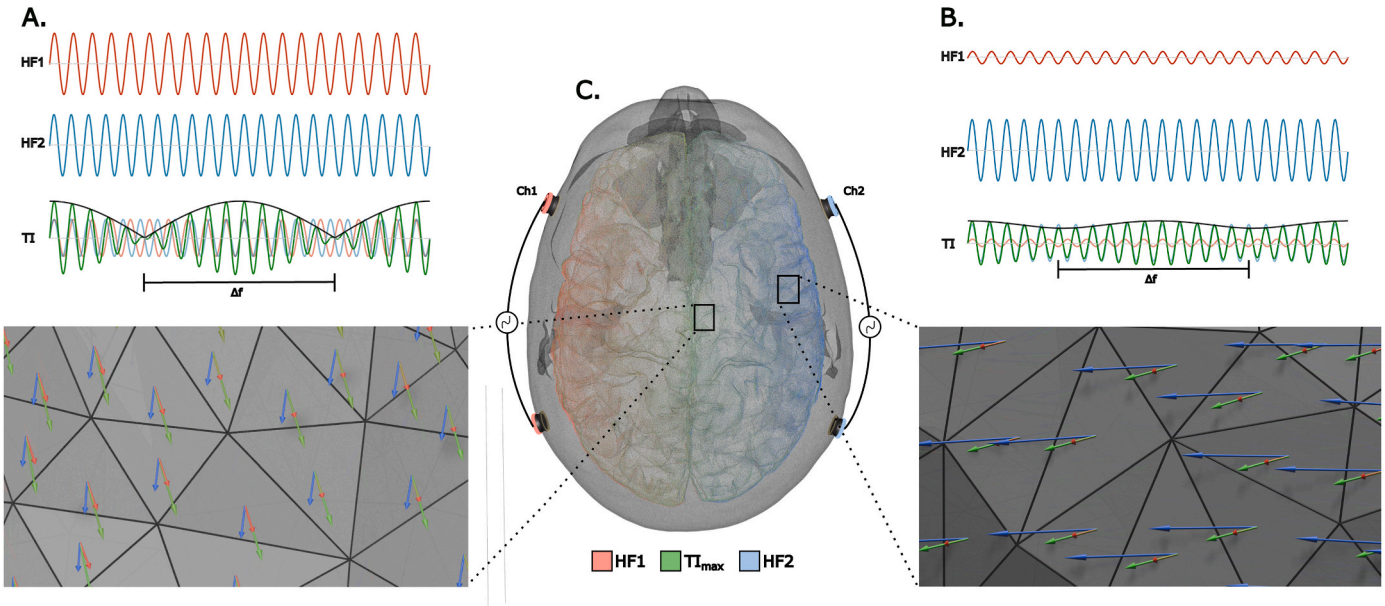

Fig. 1. Temporal and spatial characteristics of temporal interference (TI) field distribution. ***A.*** *Central brain region showing maximal modulation amplitude where TI envelope (Δf) dominates over high-frequency (HF) carrier components (HF_1,HF_2).* ***B.*** *Superficial cortical area demonstrating minimal modulation with dominant HF_2 carrier activity.* ***C.*** *Three-dimensional head model illustrating electrode montage with HF_1 (carrier frequency; red), HF_2 (carrier frequency + Δf; blue), and the calculated TI_{max} vectors (green). Vector fields reflect the electric-field magnitude and direction at each gray-matter surface element, obtained by averaging the field contributions from the three nodes defining each triangular facet.*

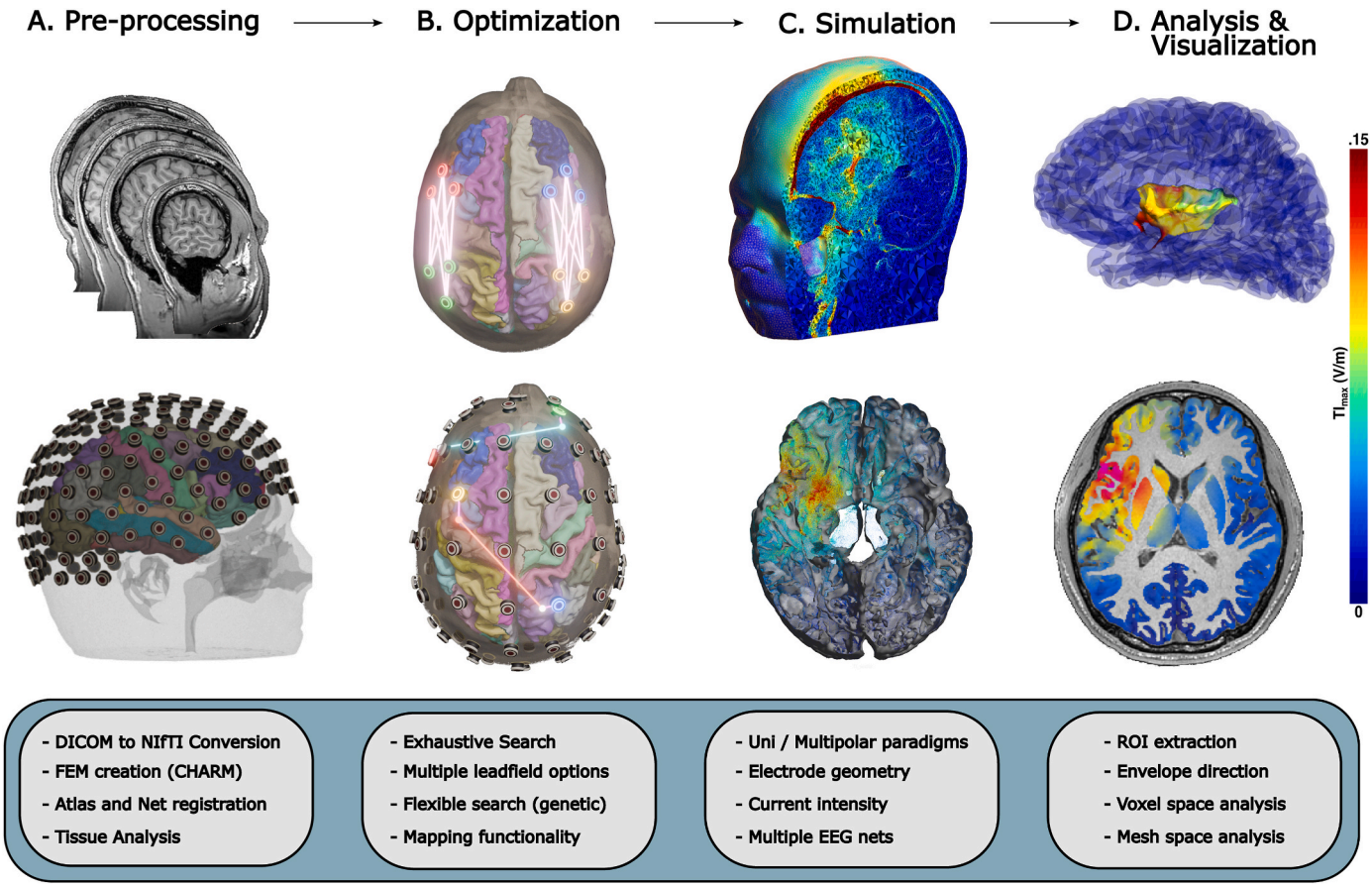

Fig. 2. TI-Toolbox integrated computational pipeline. ***A.*** *Preprocessing module: DICOM-to-NIfTI conversion* via *dcm2niix, FreeSurfer recon-all cortical reconstruction, and SimNIBS's charm for finite element method (FEM) head model generation.* ***B.*** *Optimization algorithms: flex-search genetic algorithm and exhaustive search approaches for electrode montage determination with region-of-interest (ROI) targeting.* ***C.*** *Simulation engine: magnitude and direction computation of* TI_{max}. ***D.*** *Analysis and visualization: ROI extraction, and mesh/volumetric output generation compatible with Gmsh and Freeview.*

(mesh) or volumetric (voxel) evaluation pipelines, with outputs viewable in Gmsh [31] (mesh) and Freeview [32] (voxel), and with optional cohort-level exports in MNI space.

Each component is accessible through both a command line interface (CLI) and a PyQt5-based graphical user interface (GUI) [33,34]. Containerization via Docker [35] ensures reproducibility [36] and simple orchestration of external dependencies across operating systems (Fig. 3).

2.2. Prerequisites

To utilize TI-Toolbox, users must provide anatomical MRI data in DICOM format, with at least a T1-weighted sequence required for structural processing. The inclusion of T2-weighted images is recommended to improve tissue segmentation accuracy, and diffusion-weighted imaging (DWI) data may be supplied for the computation of directional conductivity tensors for running anisotropic simulations.

The platform is compatible with Windows, Linux, and macOS operating systems via Docker-based containers running Ubuntu. Docker (or Docker Desktop) is the only required local installation; all other dependencies are encapsulated within the containerized environment.

Access to the graphical user interface requires X11 forwarding across all operating systems. For standard usage, a minimum of 32 GB RAM is recommended. Installation instructions and a detailed usage guide are available in the project's website [37].

Once prerequisites are installed, the correct Brain Imaging Data Structure (BIDS) formatting should be provided for the rest of the tools to work properly. Specifically, the user needs to set up their sourcedata sub-directory with either raw DICOMs or NIfTI files. The rest of the required files are generated automatically as the user moves through the TI-Toolbox (Fig. 3B). To facilitate immediate use and learning, TI-Toolbox natively ships with the Ernie's T1-weighted and T2-weighted scans from previous work [27] and MNI152 data [38].

2.3. Core components and implementation

2.3.1. Preprocessing pipeline

The preprocessing module orchestrates a workflow that transforms raw MRI data into simulation-ready head models through three primary stages: DICOM conversion, cortical reconstruction, and finite element method (FEM) model creation.

DICOM to NIfTI conversion is performed using dcm2niix [39], which consolidates DICOM series into volumetric images. This process produces outputs compliant with the BIDS for compatibility with downstream workflows.

Structural processing leverages FreeSurfer's recon-all pipeline [32] through the recon-all function, which performs cortical reconstruction including tissue segmentation, surface extraction, and automatic parcellation using standard atlases. The implementation supports both serial and parallel execution modes, with the parallel mode utilizing GNU Parallel [40] for efficient multi-subject processing.

Head model generation employs SimNIBS's charm function [41] for creating detailed FEM models. When both T1 and T2 images are available, charm utilizes multi-modal information for improved tissue segmentation accuracy. As part of the charm command, multiple 10–20 and high-density electroencephalogram (HD-EEG) nets are co-registered

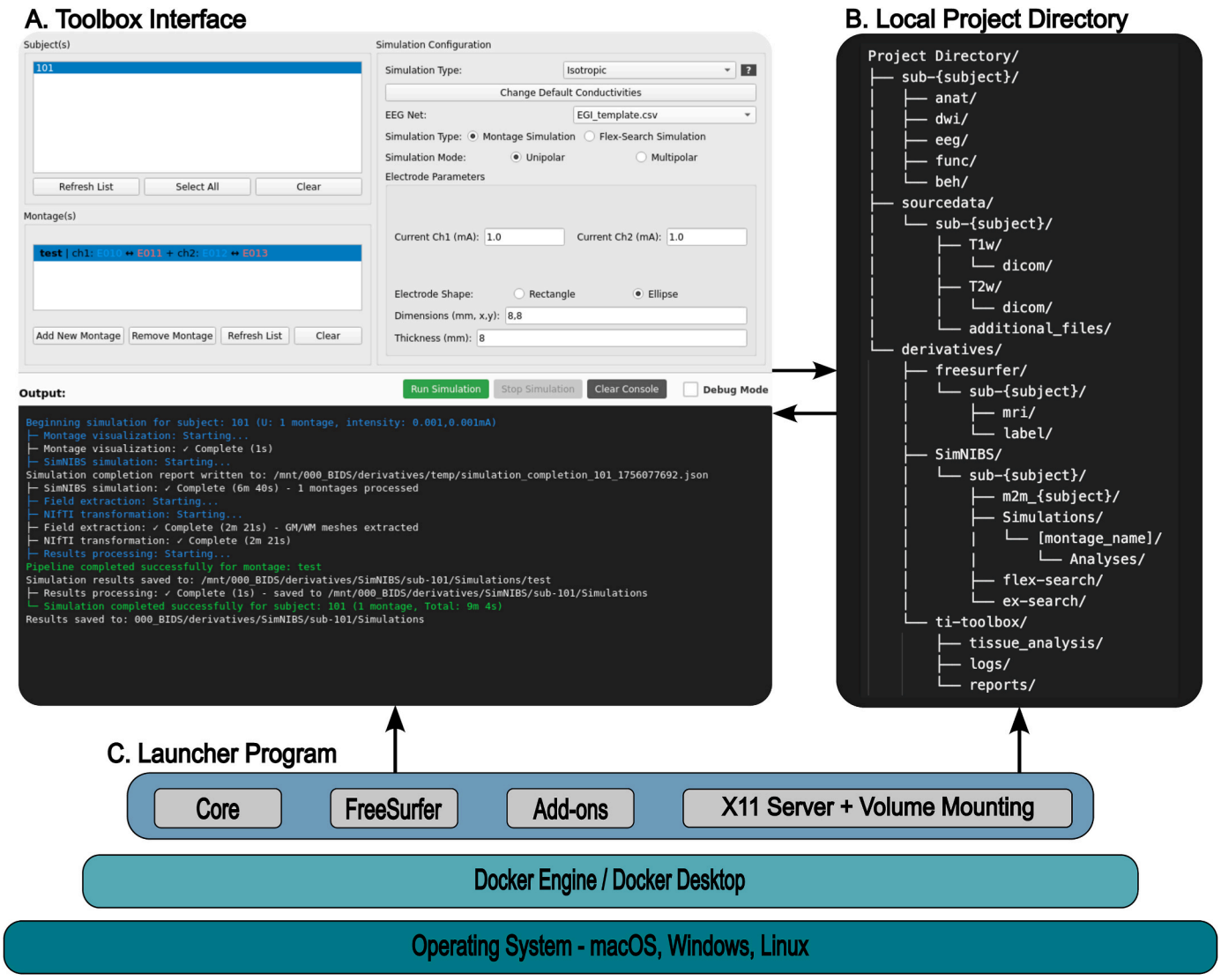

Fig. 3. TI-Toolbox software architecture and containerized deployment. ***A.*** *Unified interface providing graphical user interface (GUI) and command-line interface (CLI) access for workflow orchestration.* ***B.*** *Brain Imaging Data Structure (BIDS)-compliant project directory organization showing sourcedata/, derivatives/, and standardized file hierarchy.* ***C.*** *Multi-layered deployment architecture: host operating system supporting Docker containerization with launcher program managing SimNIBS and FreeSurfer dependencies through isolated container environments.*

with the head model via non-linear transformation from Montreal Neurological Institute (MNI) to subject space (Fig. 2A and S9). All steps incorporate comprehensive error handling, generate timestamped logs, and sharable HTML reports (section 2.4).

Following FEM model creation, a dedicated tissue analysis script estimates cortical bone morphology, ventricular and subarachnoid cerebrospinal fluid (CSF), and skin characteristics, producing subject-level metrics (Fig. 8A and B). These metrics are exported alongside preprocessing reports and can serve as covariates for downstream inter-individual variability analyses (Section 2.6.4).

2.3.2. *Optimization algorithms*

The optimization module implements two complementary approaches addressing the unique challenges of multi-electrode, multi-objective optimization in TI stimulation:

Flex-Search Algorithm: Built upon SimNIBS's TesFlexOptimization class [42], this module implements a leadfield free adaptive genetic algorithm. Flex-Search iteratively evolves electrode montages by simulating montages, evaluating the resulting electric field in a specified ROI based on a user-defined goal, and mutating to improve solutions over generations. The flex-search allows for easy and intuitive configuration of optimization parameters including goal selection (mean field, maximum field, or focality), post-processing options (TI_{max}, dir_TI_{normal}, or dir_$TI_{tangential}$), and electrode dimensions. For focality optimization, the algorithm seeks to maximize field intensity within the target region while minimizing field spread in a region defined as non-ROI. This is achieved by setting thresholds in which the ROI should exceed, and non-ROI should be kept below. This approach promotes spatial selectivity by explicitly penalizing widespread field distributions, making threshold selection a critical parameter that determines which brain regions are considered activated during optimization (Fig. S3). To mitigate local optima, the tool supports a multi-start strategy in which the optimizer is launched multiple times with distinct seeds; users can specify the number of runs and automatically retain the best montage across starts. While the multi-start approach consistently improves targeting performance, the gains are typically modest (Fig. S1).

The algorithm supports three distinct ROI definition methods through helper functions. The spherical approach enables definition of spherical ROIs with customizable center coordinates and radii, ideal for targeting specific anatomical landmarks. The atlas based approach

interfaces with cortical atlases (Desikan-Killiany, Destrieux, HCP-MMP1) [43–45] to target specific cortical regions by label. The sub-cortical approach extends targeting capabilities to volumetric subcortical structures using the charm labeling.nii.gz output. The implementation also provides control over hyper-parameters including maximum iterations, population size, and CPU core utilization for performance tuning.

The electrode mapping functionality utilizes an optimal assignment algorithm to project unconstrained optimization solutions onto standard EEG montages. The method constructs a Euclidean distance matrix between the optimized electrode positions and available positions from co-registered EEG nets. The Hungarian algorithm via scipy.optimize.linear_sum_assignment then solves the bipartite matching problem to minimize total assignment distance while ensuring a one-to-one mapping between optimized and standard positions (Fig. 4A and S5) (Table S1).

Local Search Algorithm: The module relies on a pre-computed leadfield and performs systematic evaluation of montages through cartesian product operations, ensuring a logical balance between coverage of the search space and compute efficiency (Fig. 2B top). Critically, the ex-search algorithm includes per-channel current optimization as a decision variable, systematically evaluating current ratios, ensuring comprehensive exploration of both electrode positions and current distributions. Results are stored in a.csv file that includes intensity and focality metrics for the user to inspect (Table S2).

The local search evaluates possible electrode montages and current distributions according to:

$$N_{total} = N_{elec}^{4} \cdot N_{current}$$

where: N_{elec} is the number of electrode candidates per position, N_{elec}^{4} accounts for selecting electrodes at four positions E_1^+, E_1^-, E_2^+, and E_2^- and $N_{current}$ is the number of current ratio combinations.

Valid current combinations satisfy:

$$N_{current} = \left\{ (I_1, I_2) : \begin{matrix} I_1 + I_2 = I_{total} \\ I_{step} \le I_1, I_2 \le I_{limit} \end{matrix} \right\}$$

2.3.3. Simulation engine

The simulation module offers a robust control over simulation parameters which interfaces with SimNIBS's sim_struct.SESSION class to configure parameters like anisotropy type (scalar, volume normalized, directional), electrode geometries, and current delivery.

For TI calculation, the module leverages SimNIBS internal functions to compute individual electric fields for each carrier frequency pair. These fields are then processed through the TI_utils.get_maxTI() function, which implements the formula suggested by Grossman et al., 2017 [1].

In addition to TI_{max}, which is defined as the maximum envelope modulation vector, a surface-aligned normal component (TI_{normal}) is computed from the local TI_{max} vector onto the middle layer of the gray-matter surface (Fig. 4C). Both TI_{max} and TI_{normal} are exported and

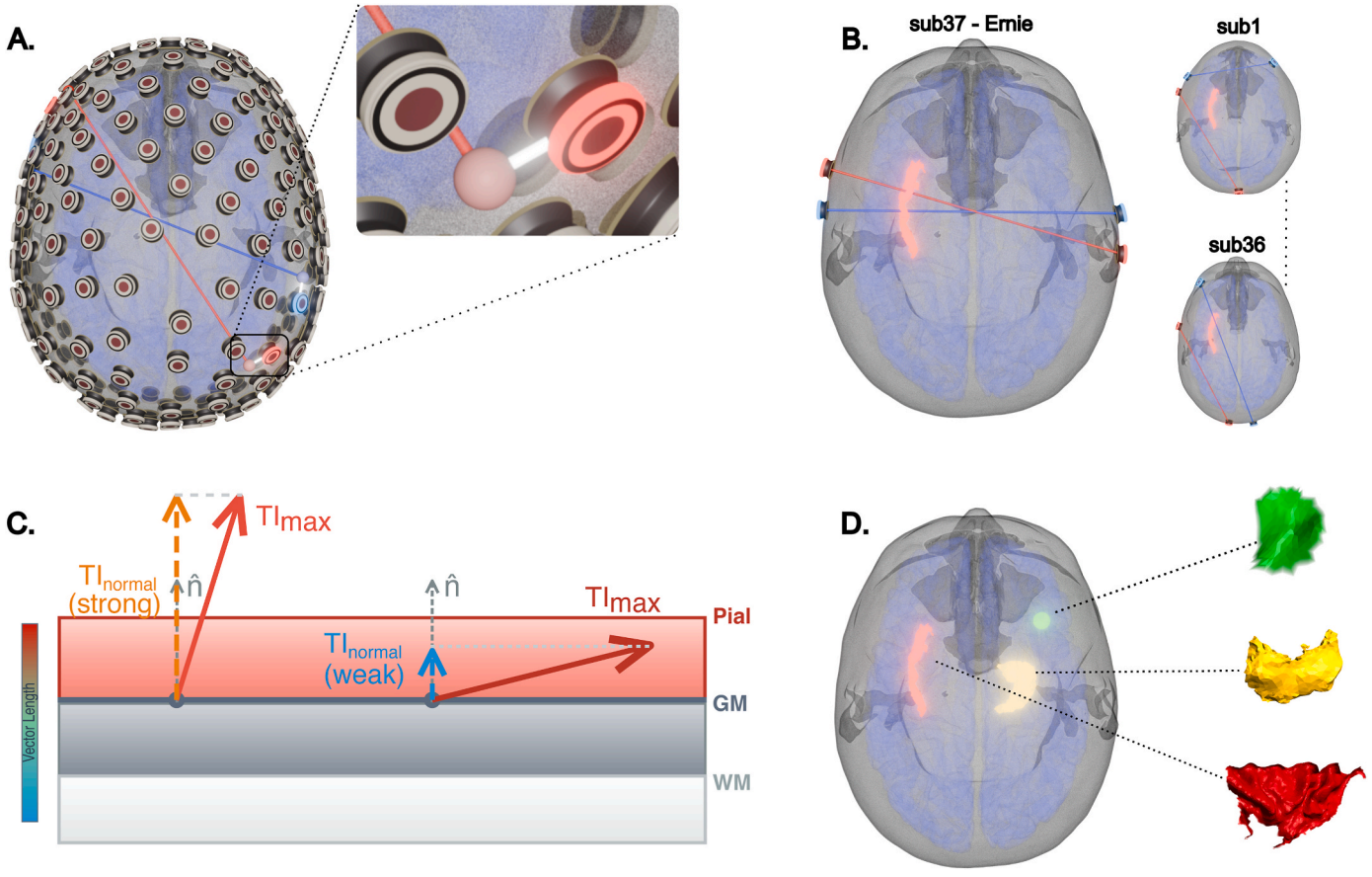

Fig. 4. Target definition and optimization objectives for case studies. ***A.*** *Electrode mapping functionality demonstrating unconstrained optimization to standard high-density electroencephalography (HD-EEG) net projection using Hungarian algorithm for optimal electrode assignment.* ***B.*** *Head model comparison between subject-specific anatomical models (subjects 1–36) and generalized template (Ernie model, subject 37).* ***C.*** *Vector illustrations: TI_{max} (maximal modulation) and TI_{normal} (surface-aligned normal component) vectors relative to the middle layer surface of the gray matter.* ***D.*** *Target regions: left insula (cortical, red), right hippocampus (subcortical, yellow), and spherical ROI (green) at Montreal Neurological Institute (MNI) coordinates (36.10, 14.14, 0.33) with* 5 mm *radius, representing diverse anatomical targeting scenarios. The hippocampus originates from voxel-based volumetric segmentation (aseg) while the insula (DKT atlas) and the spherical targets are surface based. Magnified panels depict re-oriented and zoomed views of each ROI to highlight their morphology.*

analyzed downstream as part of the analyzer tool.

Output management includes generation of both volumetric and surface-mapped results, with automatic conversion to MNI space for group-level analyses and visualizations. The module creates visualization files compatible with Gmsh and Freeview, facilitating immediate inspection of simulation results in mesh and voxel spaces.

Additionally, the platform implements multi-channel TI approach for montages that involve more than two electrode pairs (multi-polar TI) [46] This extension supports emerging TI stimulation paradigms that utilize more than two channels to achieve enhanced spatial selectivity, steering, or multi-target stimulation (Fig. S2). For multi-polar TI, the maximal modulation vectors (TI_{max}) from TI_A and TI_B are fed back into Grossman's analytical formula to find the TI_{AB} vector.

For reproducibility and batch processing, all electrode montages are saved to and loaded from a centralized montage database montage_list.json that maintains both unipolar and multipolar montage definitions for various EEG cap systems.

High-Frequency Field Assessment: The simulator outputs detailed analysis of the individual carrier fields before interference calculation. A summary statistics file documents key metrics including mean, maximum, and percentile values for each carrier field within gray matter. Specific Absorption Rate (SAR) can be derived from this output according to the safety recommendations from Cassarà et al., 2025 [19,20] which will be integrated in future version of the TI-Toolbox.

All outputs maintain consistent naming conventions incorporating subject identifiers, target names, and field types, facilitating automated processing in downstream pipelines. The modular output structure supports selective export based on computational resources and research needs, with options to disable specific output types through configuration parameters.

2.3.4. Analysis and visualization

The analysis module provides tools for quantifying and visualizing TI stimulation outcomes through the MeshAnalyzer class. This class implements three primary analysis modes: spherical ROI analysis, cortical region analysis, and whole-head analysis. The spherical analysis method utilizes SimNIBS's mesh manipulation functions to extract field values within specified coordinates and radii. For cortical analysis, the class interfaces with multiple anatomical atlases through SimNIBS's subject_atlas() function, supporting Desikan-Killiany, Destrieux, and HCP-MMP1.

A surface mesh generation pipeline calls the msh2cortex utility to project volumetric field data onto the middle layer of the cortex. This enables accurate analysis of field distributions in gray matter while accounting for cortical folding patterns (Fig. 2D top). Visualization capabilities are implemented through the MeshVisualizer class, which generates multiple output formats including 3D mesh visualizations with customized colormaps (viewable in Gmsh), ROI weighted field distribution histograms, and region-wise scatter plots.

For volumetric analysis, the VoxelAnalyzer class provides complementary functionality for analyzing field distributions in NIfTI format. This includes both spherical and atlas-based ROI extraction which can be inspected in Freeview (Fig. 2D bottom).

Group-level analysis enables collection and comparison of TI simulation results across multiple subjects. This module generates averaged volumetric field distributions in NIfTI format, producing inter-subject comparison plots, and exporting summary statistics across the cohort. Group level analysis remains in subject space for cortical and subcortical regions while arbitrary spherical targets are defined in MNI space and automatically transform into each subject's native space using SimNIBS 'mni2subject_coords' method.

Beyond these built-in routines, the TI-Toolbox also provides utilities for exporting cortical surfaces and field distributions for use in external 3D modeling environments such as Blender [47]. Subject-specific cortical surfaces generated during preprocessing can be exported either as.stl files for geometric visualization or as.ply surfaces that retain both cortical geometry and corresponding TI field magnitudes. The TI-Toolbox also supports exporting surface-aligned 3D vector representations of the different fields, allowing direction and intensity information to be visualized directly on the cortical surface in external rendering tools. These export features were used to produce the surface-based figures presented in this work.

2.4. Standardization and reproducibility

TI-Toolbox aims to ensure complete reproducibility and standardization across clinical research workflows. The platform's logging infrastructure provides consistent formatting and hierarchical logging across all components. The logger creates timestamped log files following the pattern [YYYY-MM-DD HH:MM:SS] [module_name] [level] message, ensuring precise tracking of all operations.

The logger communicates with external dependencies including SimNIBS, and FreeSurfer, redirecting their outputs through the platform's unified logging system. This integration ensures that all processing steps, regardless of their origin, are captured in a single, searchable log file stored in the BIDS-compliant [48] directory structure. A complimentary feature creates HTML reports that summarize key processes and outcomes similar fMRIPrep [49], documenting aspects of the pipeline.

2.5. Deployment and infrastructure

2.5.1. Docker compose

TI-Toolbox's deployment architecture leverages Docker Compose orchestration to manage a complex ecosystem of neuroimaging tools while ensuring consistent behavior across diverse computing environments. The docker-compose.yml configures the primary service containers: Core (+SimNIBS), FreeSurfer, connected through a dedicated bridge network (Fig. 3C).

Volume management is handled through named Docker volumes that persist software installations across container restarts, significantly reducing startup times. The LOCAL_PROJECT_DIR environment variable enables flexible data mounting, allowing users to process data stored anywhere on their filesystem while maintaining isolation between the host and container environments.

2.5.2. Launcher program

TI-Toolbox implements several deployment strategies to accommodate different use cases:

Desktop Deployment: The executable launcher provides platform-specific binaries created through Electron [50]. The launcher includes error handling providing user-friendly feedback for common issues such as Docker daemon availability and permission errors. The launcher requires no technical expertise or an extensive installation process - users simply download the file from the release page [37], double-click to install, and launch the GUI. Docker Desktop installation is similarly straightforward.

Server Deployment: The bash-based launcher loader.sh implements a deployment script that handles the setup necessary for healthy operation of the TI-Toolbox. The bash entry point provides a solution for headless servers processing and can be used as a desktop alternative to the executable approach.

2.5.3. Batch processing and parallelization

TI-Toolbox implements batch processing and parallelization strategies to enable efficient analysis of large clinical cohorts. The platform's parallelization architecture operates at multiple levels, from individual processing steps to cohort-wide analyses.

Subject-Level Parallelization: The preprocessing pipeline implements GNU Parallel integration [40] for concurrent processing of multiple subjects. When invoked with the parallel flag, the system automatically detects available CPU cores and distributes subjects across

parallel workers.

Algorithm-Level Parallelization: The flex-search optimization module supports multi-core execution through the CPUs parameter, which is passed directly to SimNIBS's differential evolution optimizer for faster processing.

Pipeline-Level Batch Processing: The GUI employs multi-threading to keep the interface responsive while long-running jobs are carried out in background worker threads. A job queue coordinates preprocessing, optimization, simulation, and analysis tasks, with real-time progress reporting, log streaming, and graceful cancellation. This design allows concurrent execution of independent stages across subjects while preserving deterministic logging and outputs.

TMUX Parallelization: The code container which is exposed to the user interaction comes with TMUX [51] installed which enables further multiplexing where the user can span multiple instances of the TI-Toolbox simultaneously.

System Monitoring: To monitor the system during high-demand processes, a designated System Monitor tab is available that tracks CPU and memory usage of the TI-Toolbox processes in real time.

2.6. Case studies

2.6.1. Targets and goals

Using the flex-search optimization algorithm, we evaluated three distinct brain targets (Fig. 4D) with specific optimization objectives. For the left insula based on DKT atlas [43] (deep cortical target) we performed two optimization rounds: (1) TI_{max} optimization maximizing the mean field intensity within the ROI, and (2) TI_{normal} optimization maximizing the mean surface-aligned normal component within the ROI. Both approaches focused on mean rather than maximum values to promote homogeneous field distributions across the target region, avoiding hotspots that may be more suitable for sub-regions (Fig. S7). Then, for the right hippocampus based on FreeSurfer's aseg tool [32] (subcortical target): we optimized for TI_{max}, maximizing the mean field intensity within the ROI. Given that it is a sub-cortical target, we focused solely on intensity optimization without additional directional constraints as subcortical structures lack the systematic columnar organization of cortex. Lastly, for the spherical ROI (centered at MNI coordinates 36.10, 14.14, 0.33; radius 5 mm): We implemented three distinct optimization strategies: (1) mean optimization maximizing the mean TI_{max} intensity within the ROI, (2) focality optimization maximizing the ratio between mean TI_{max} in the ROI versus mean TI_{max} in gray matter using various thresholding approaches, and (3) max optimization maximizing the maximum value of the TI_{normal} component within the ROI. For the complete target x goal combination diagram please see Fig. S6 in the supplementary information.

2.6.2. Subjects

We collected MRI scans of thirty-six participants (mean age = 29.9 ± 9.7 years, 58.3 % Female) from the STRENGTHEN clinical trial (Table S4). Participants were excluded if they had any neuroradiologist-identified brain structural abnormalities. All participants gave written informed consent in accordance with the University of Wisconsin-Madison Institutional Review Board. MRI data were collected using a 3 T MAGNUS (Microstructure Anatomy Gradient for Neuroimaging with Ultrafast Scanning, GE Healthcare) head-only MRI scanner. Structural images were acquired using T1-and T2-weighted images, with 0.8 mm isotropic voxels, and the following parameters. T1-weighted: sequence = MP-RAGE (Magnetization-Prepared Rapid Gradient-Echo), repetition time (TR) = 2000 ms, echo time (TE) = 3 ms, inverse time (TI) = 1100 ms, flip angle = 8°, field of view (FOV) = 256 × 256 mm2, matrix size = 320 x 320 pixels, resolution = 0.8 mm × 0.8 mm x 0.8 mm, number of slices = 240, acquisition time = 4 min. T2-weighted: sequence = CUBE-T2, TR = 2500 ms, TE = 90 ms, echo train length (ETL) = 120, FOV = 256 × 256 mm2, matrix size = 320 x 320 pixels, resolution = 0.8 mm × 0.8 mm x 0.8 mm, number of slices = 240, acquisition time = 4 min. Our 37th participant which serves as our generalized model is the publicly available Ernie model.

2.6.3. Flow

Raw DICOM files were preprocessed as in Section 2.3.1. For each target and objective, we ran the flex-search optimizer with the ROI definitions in Section 2.6.1, using a three-run multi-start configuration and retaining the best solution per subject (configurable via Advanced Settings: Number of Optimization Runs). We tested 1, 3, and 5 multi-starts on the entire cohort for the hippocampus target. The improvement plateaued after 3 starts, leading us to select 3 as optimal balance between performance and computation time (Fig. S1). Notably, we chose to follow the hyper-parameter suggested by Weise et al., 2025 during our optimization process; popsize = 13, tol = 0.1, mutation= (0.01,0.5), recombination = 0.7 [42,52].

To address Q1, we performed two simulations for each combination of subject, target, and optimization goal: one using the freely optimized montage and another using the HD-EEG mapped montage (Fig. 5). For Q2, we first optimized montages on the general head model (Ernie) for each target-goal combination, then applied these general montages to all individual subjects. We subsequently compared the performance of these general model montages against individually optimized montages to assess the impact of head model individualization on TI optimization outcomes (Fig. 6). Our simulation utilized default isotropic conductivities [53–55] (Table S3), 1 mA per channel, 8 mm electrode diameter, 4 mm thick saline gel and a 2 mm thick rubber electrode on top. Finally, we applied group analysis to extract TI_{max}, TI_{normal}, and focality within ROIs and gray matter.

For focality optimization, we evaluated three distinct thresholding strategies to assess their impact on spatial selectivity. We compared: (i) fixed absolute thresholds (0.1 V/m and 0.3 V/m) based on similar field strengths reported in the literature [2,42], (ii) adaptive threshold at 50 % of achievable peak field intensity, and (iii) adaptive threshold at 80 % of achievable peak field intensity. For adaptive approaches, a two-pass optimization strategy was employed: first, a mean TI_{max} optimization determined the achievable field intensity in the target ROI; second, a focality optimization informed by achievable values. The lower threshold was set at a constant 20 % of the achievable intensity while the upper threshold was set at the specified percentage (50 % or 80 %). This adaptive strategy ensures that focality constraints are tailored to individual head geometry and target location rather than applying potentially inappropriate fixed values that may lead a lower achieved objective value. After optimization and simulation steps were completed, we used the analyzer tools to assess field exposures in the model according to:

$$TI_{mean}^{ROI} = \frac{1}{N}\sum_{j\in ROI} TI_{max}(j) \quad \text{Focality} = \frac{TI_{mean}^{ROI}}{TI_{mean}^{GM}}$$

Where $TI_{max}(j)$ is the TI modulation amplitude at mesh element j and TI_{mean}^{GM} follows the same formulation as TI_{mean}^{ROI} with ROI being the entire gray matter.

2.6.4. Statistical analysis

Statistical analyses were conducted using Python with scipy, statsmodels, and pandas libraries. Data normality was assessed using the Shapiro-Wilk test scipy.stats.shapiro, with parametric paired *t*-test via scipy.stats.ttest_rel or non-parametric Wilcoxon signed-rank test via scipy.stats.wilcoxon approaches selected based on normality test results ($p > 0.05$ indicating normal distribution. To control for multiple comparisons, we employed the Benjamini-Hochberg (BH) false discovery rate (FDR) correction procedure [56]. Within each research question (e.g., optimized vs. mapped stimulation, Ernie vs. mapped stimulation), all p-values from primary, parametric, and nonparametric tests across all variables were grouped as a single family for correction, with each question corrected independently. Significance levels are reported as

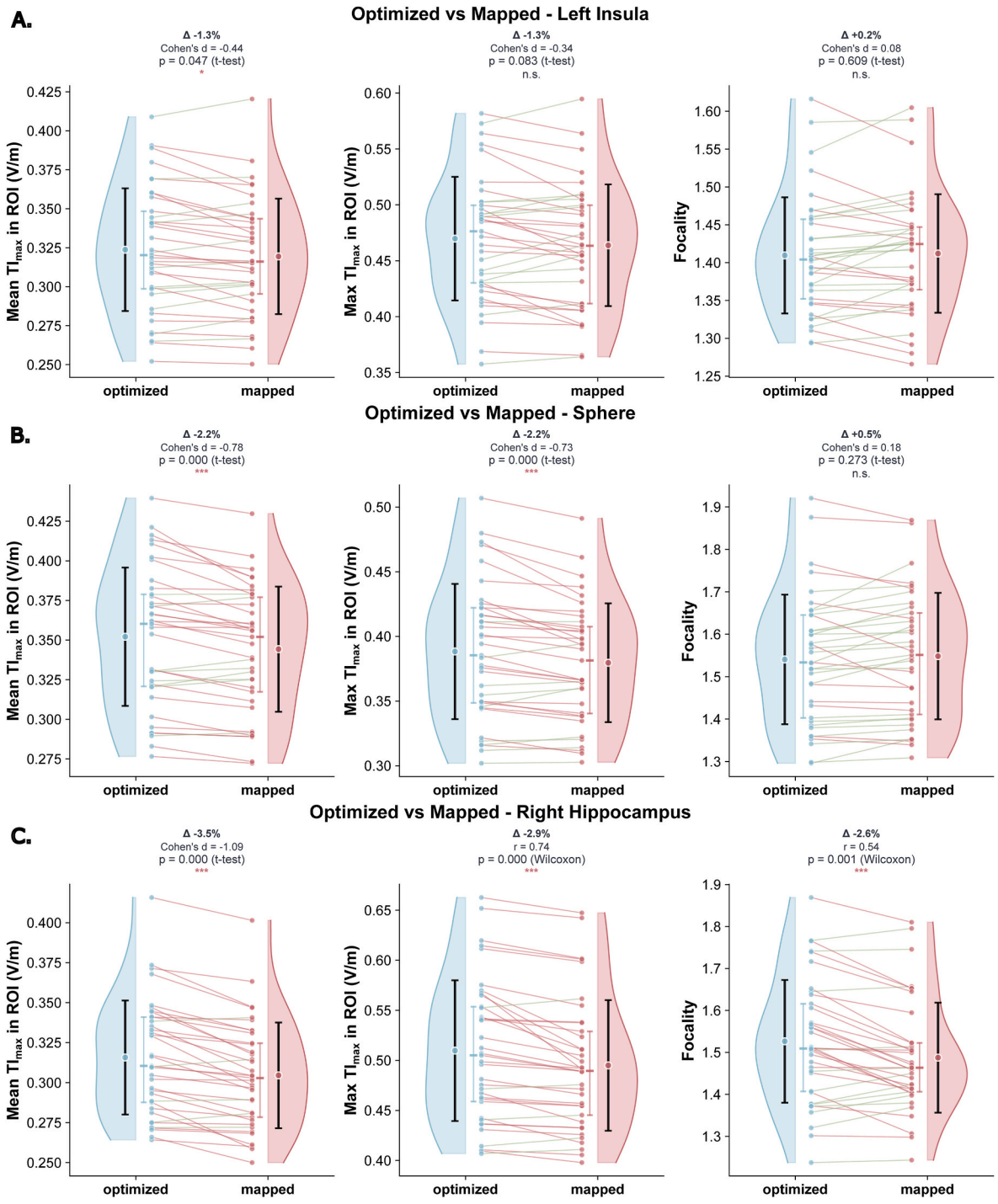

Fig. 5. Comparison of optimized versus mapped electrode montages. **A.** Within-subject comparison for left insula of TI_{max} characteristics between 'optimized' and 'mapped' conditions: mean TI_{max} = 0.324 vs 0.319 V/m ($\Delta = -1.33$ %, $p = 0.047$), maximum TI_{max} = 0.470 vs 0.464 V/m ($\Delta = -1.26$ %, $p = 0.083$), focality preserved ($\Delta = 0.18$ %, $p = 0.609$). **B.** Spherical target results: mean TI_{max} reduction of −2.22 % ($p = 9.58 \times 10^{-5}$), maximum TI_{max} reduction of −2.24 % ($p = 0.0001$), focality unchanged ($p = 0.273$). **C.** Right hippocampus analysis: mean TI_{max} reduction of −3.53 % ($p = 3.20 \times 10^{-7}$), maximum TI_{max} reduction −2.89 % ($p = 1.48 \times 10^{-6}$), and focality reduction of −2.55 % ($p = 0.0006$). Colored lines connect paired observations from the same participant (green for increase, red for decrease, gray for no change), illustrating individual response to different montage conditions (n = 37). Half violin plots show density distributions. Colored circles represent group means with black vertical lines indicating ±SD while rectangles with vertical lines indicate interquartile range (IQR). Statistical comparisons were performed using paired *t*-test or Wilcoxon signed-rank test with significance denoted as: $p < 0.001$, $p < 0.01$, $p < 0.05$, n.s. = not significant. Effect size (Cohen's d/r) and percentage change are displayed above each comparison. TI_{max} are expressed as V/m.

follows: *$p < 0.05$, **$p < 0.01$, and ***$p < 0.001$.

Effect sizes were calculated using Cohen's d for parametric tests (computed as mean difference divided by pooled standard deviation) and r ($Z/\sqrt{N}$) for non-parametric tests, where Z-scores were obtained from the Wilcoxon test statistic. Practical effect sizes were reported by computing the percent change between the two groups $\Delta\% = \frac{\overline{B_i - A_i}}{\overline{A}} \cdot 100\%$ and magnitude of within-subject variability as $\Delta\% =$

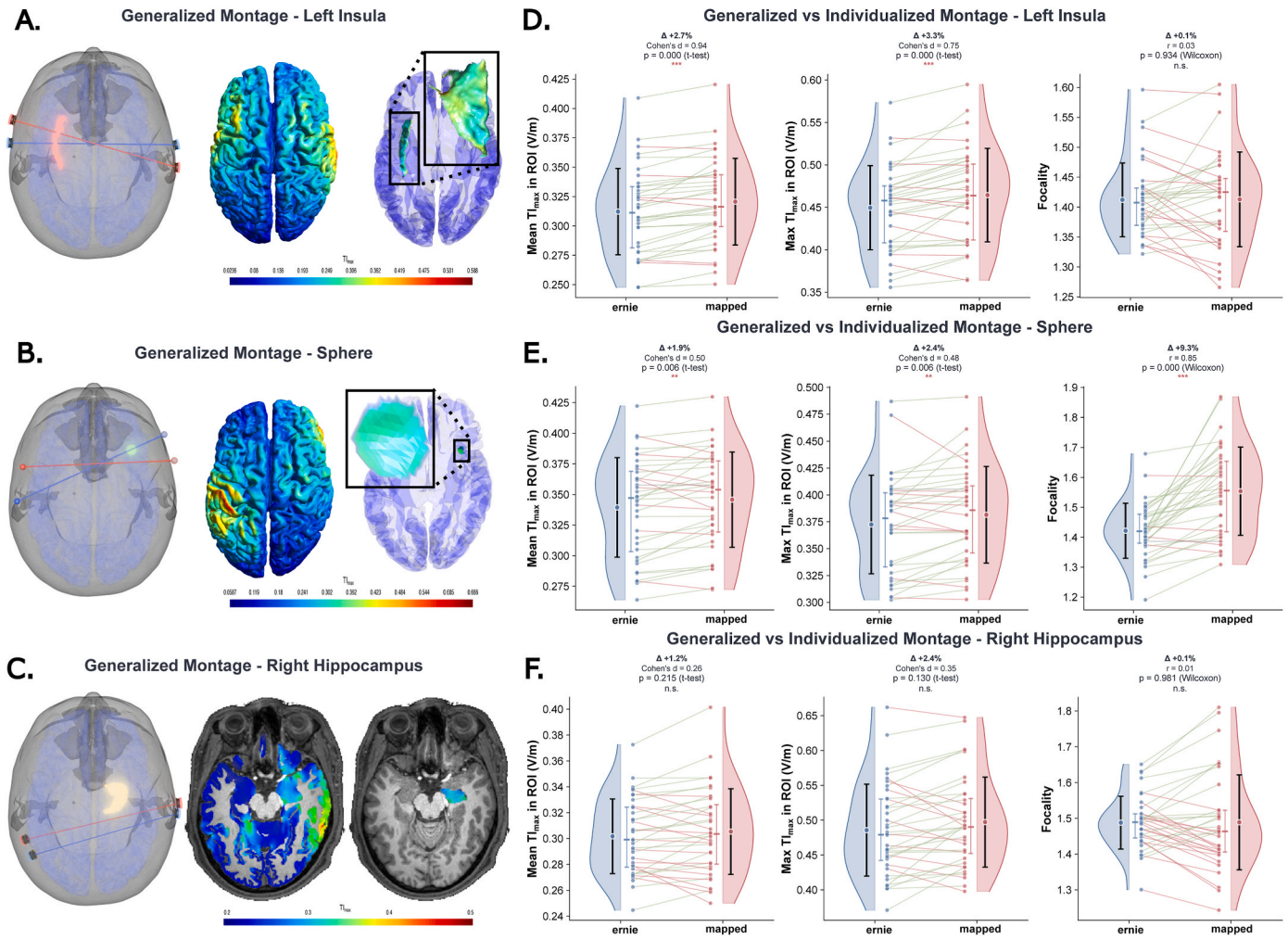

Fig. 6. Individualized versus generalized head modeling performance. **A-C.** *On the left, montages suggested by the generalized model (subject 37, Ernie) for the Left insula, sphere, and right hippocampus. On the right, cortical field distribution and extracted ROI for subsequent analyses.* **D.** *Left Insula comparison: subject-specific suggested mapped montages (red dots) versus generalized template montage (Ernie, blue dots). Individualized models achieved higher mean* TI_{max} *(+2.70 %,* $p = 6.51 \times 10^{-6}$*) and maximum* TI_{max} *(+3.31 %,* $p = 9.88 \times 10^{-5}$*) compared to template.* **E.** *Spherical comparison: Individualized models showed modest advantages in maximum field (+1.86 %,* $p = 0.006$*) and superior focality (+9.3 %,* $p = 1.75 \times 10^{-6}$*).* **F.** *Right hippocampus comparison in volumetric space: Comparable field intensities between approaches (mean* TI_{max} *+1.21 %,* $p = 0.213$*; maximum* TI_{max} *+2.38 %,* $p = 0.130$*) with no significant difference in focality (+0.07 %,* $p = 0.981$*). Colored lines connect paired observations from the same participant (green for increase, red for decrease, gray for no change), illustrating individual response to different montage conditions (n = 36). Half violin plots show density distributions. Colored circles represent group means with black vertical lines indicating ±SD while rectangles with vertical lines indicate interquartile range (IQR). Statistical comparisons were performed using paired t-test or Wilcoxon signed-rank test with significance denoted as: p < 0.001, p < 0.01, p < 0.05, n.s. = not significant. Effect size (Cohen's d/r) and percentage change are displayed above each comparison.* TI_{max} *are expressed as V/m.*

$\frac{\overline{|B_i - A_i|}}{\overline{A}} \cdot 100\%$ where A and B represent the two conditions being compared.

For inter-individual variability analyses (Q3), we investigated anatomical determinants of TI field exposure using data from the optimized electrode montages. First, we assessed multicollinearity among anatomical predictors (age, bone thickness/volume, CSF thickness/volume, and skin thickness/volume) using correlation analysis. Based on high correlations within tissue types, we selected volume measures over thickness to reduce multicollinearity while retaining predictive information. Volumetrics were extracted from labeling.nii.gz file produced during subjects' pre-processing, which thresholds the images on the Z axis based on the top of the brainstem (Fig. 8A and B). Then, the sum of voxels belonging to desired tissue and above said threshold were multiplied by their volume extracted from the NIfTI header using nibabel package [57]. We then employed multiple linear regression (MLR) model constructed using statsmodels.api.OLS with ordinary least squares fitting to quantify the overall variance explained by anatomical factors $TI_{mean}^{ROI} = \beta_0 + \beta_1 \cdot Age + \beta_2 \cdot V_{bone} + \beta_3 \cdot V_{CSF} + \beta_4 \cdot V_{skin} + \epsilon$. Model fit was evaluated using R^2, adjusted R^2, and F-statistics. The models were applied separately to the left insula, right hippocampus and spherical targets.

3. Results

3.1. Overview

We investigated TI field characteristics across three distinct brain targets in a cohort of 37 participants. To provide useful benchmarks for the community we compiled the typical time required for TI-Toolbox operations and hardware load (Table 1). For the left insula (deep cortical target), we evaluated solutions from both TI_{max} optimization (maximizing mean field intensity) and TI_{normal} optimization (maximizing mean surface-aligned normal component). The right hippocampus (subcortical target) was analyzed using TI_{max} optimization focused on maximizing mean field intensity. The spherical ROI (MNI coordinates 36.10, 14.14, 0.33; radius 5 mm) was evaluated using three

Table 1
Components and performance of TI-Toolbox on a MacBook Pro (2023, Apple Silicon M2 Max, 32 GB RAM). Benchmark results include computation times for key functions, memory usage, and typical workflow performance to illustrate efficiency and scalability.

Module	Primary Inputs	Primary Outputs	Runtime per Subject	Memory Peak (GB)	Notes
Preprocessing					
DICOM Conversion	Raw DICOM series (T1w, T2w)	BIDS-compliant NIfTI files	sec	0.3	single core (83.4 % CPU)
Reconstruction (recon-all)	T1w/T2w-weighted NIfTI	Tissue segmentation, surface meshes, cortical parcellations	3h 44m	2.2	single core (68.6 % CPU)
FEM Generation (CHARM)	T1w/T2w NIfTI	FEM head model (.msh), co-registered EEG nets, labeling.nii.gz	1h 10m	8.4	multi-core (640.4 % CPU)
Tissue Analysis	labeling.nii.gz	Bone/CSF/skin metrics	24s per tissue	0.44	single core
Leadfield Generation	FEM model, EEG montage definition	Pre-computed leadfield matrix	Variable	Variable	single core
EEG10-20	FEM model, Okamoto 2004 coordinates	Leadfield matrix (21 electrodes)	2m 34s	2.0	electrodes, single core (97.4 % CPU)
EEG10-10	FEM model, UI Jurak 2007 coordinates	Leadfield matrix (75 electrodes)	18m 3s	7.1	electrodes, single core (92.6 % CPU)
EEG10-5	FEM model, GSN-HydroCel-185 coordinates	Leadfield matrix (183 electrodes)	46m 23s	7.4	electrodes, single core (95.1 % CPU)
Optimization					
Flex-Search (Genetic)	FEM model, target ROI, goal function, opt parameters	Optimized electrode positions, field metrics	40m 33s	9.7	Genetic algorithm, 3 multistarts, single core (101.5 % CPU)
Local-Search (Cartesian Product)	Pre-computed leadfield, EEG candidates, current parameters, target ROI	CSV of montage-current combinations, intensity/focality metrics	Variable	4.0	Leadfield-based, single core
2 electrodes	Leadfield, electrode-current combinations	112 evaluations	1m 27s	4.0	single core (85.2 % CPU)
4 electrodes	Leadfield, electrode-current combinations	1792 evaluations	10m 23s	4.0	single core (102.2 % CPU)
6 electrodes	Leadfield, electrode-current combinations	9072 evaluations	50m 46s	4.0	single core (100.5 % CPU)
Electrode Mapping	Optimized positions, standard EEG coordinates	Mapped positions to standard nets	–	–	Post-optimization mapping
Simulation					
TI Field Computation	FEM model, electrode montage, electrode/current/anisotropy parameters	TI_{max}/TI_{normal} fields (volumetric & surface), carrier fields, MNI outputs, visualizations	11m 58s	3.4	Complete pipeline, single core (56.1 %)
Montage visualization	Electrode positions on EEG net	Electrode placement visualization	2s	–	Electrode placement check
SimNIBS simulation	FEM model, electrode montage	FEM-solved electric fields (2 pairs)	8m 56s	3.4	FEM simulation
FEM assembly/solving	FEM model, current injection	Solved electric field per pair	2m per pair	–	Per electrode pair
Volume interpolation	Surface fields, gray matter mask	Volumetric gray matter field map	4m 55s	–	Gray matter interpolation
NIfTI conversion	Mesh fields, anatomical T1	MNI-transformed field volumes	2m 52s	–	MNI transformation
T1 to MNI	Subject T1, MNI template	Registration transformation	12s	–	Anatomical registration
Mesh to NIfTI	Field meshes, transformation	Field volumes in MNI space	2m 40s	–	Field volume creation
Results processing	Simulation outputs	Organized output files	1s	–	File organization
Analysis & Visualization					
Mesh Analyzer	Surface-mapped fields (.msh), ROI, atlas	Surface-based statistics, 3D visualizations (Gmsh)	35s	0.44	Sphere and cortical atlases
Voxel Analyzer	Volumetric fields (NIfTI), ROI, atlas	Voxel-wise statistics, visualization (Freeview)	7s	0.31	Volume-based analysis, sphere ROI
Group Analyzer	Multi-subject TI results, MNI/subject coordinates	cohort statistics, MNI maps	Variable	–	Multi-subject analysis
System Components					
Logging & Reports	All module operations, pipeline execution data	Timestamped logs, HTML preprocessing/simulation reports	–	–	Automatic documentation
Deployment	Docker Engine/Docker Desktop, user data directories	Containerized environment, CLI/GUI (PyQt5), cross-platform compatibility	–	–	Docker-based deployment
TOTAL PIPELINE	**Raw DICOM to analyzed TI fields**	**Complete analysis-ready outputs**	**5–6 h**	**9.7**	**Minimum 16 GB RAM recommended**

TI-Toolbox: Components, Inputs, Outputs, and Performance Benchmarks.

optimization strategies: mean TI_{max} intensity, focality (ratio of mean TI_{max} in ROI to gray matter), and maximum TI_{normal} component. All statistical comparisons employed paired tests selected based on normality assessments (two-tailed $\alpha = 0.05$), with effect sizes and percentage changes calculated to evaluate both statistical and practical significance.

3.2. Mapping optimized solutions to HD-EEG

To assess whether constraining electrode placements to standard HD-EEG positions compromises optimization benefits, we compared field characteristics between freely optimized montages (optimized) and their mapped counterparts (mapped) across all three targets ($n = 37$, including the generalized model subject). These analyses focus on the

mean optimization results—maximizing mean TI_{max} intensity for the left insula, right hippocampus, and spherical ROI. For the left insula, mapping to standard electrode positions resulted in minimal yet statistically significant impact with mean TI_{max} (−1.33 %, p = 0.047, |Δ| = 2.55 %, d = −0.44) and maximum (−1.26 %, p = 0.083, |Δ| = 3.07 %, d = −0.34) field metrics showing small reductions that did not reach significance. Focality also remained unchanged 1.40 vs 1.41 (+0.17 % p = 0.609, |Δ| = 1.63 %, d = 0.08), suggesting that spatial selectivity was preserved (Fig. 5A). For the spherical target, mapping decreased mean TI_{max} from 0.352 V/m to 0.344 V/m (−2.22 %, $p = 9.58 \times 10^{-5}$, |Δ| = 2.73 %, d = −0.79), with maximum values showing similar reductions from 0.388 V/m to 0.380 V/m (−2.25 %, p = 0.0001, |Δ| = 2.86 %, d = −0.74). However, focality remained statistically unchanged 1.541 vs 1.548 (+0.505 %, p = 0.273, |Δ| = 2.06 %, d = 0.19), reinforcing that electrode mapping preserves targeting precision (Fig. 5B). The right hippocampus demonstrated stronger sensitivity to the mapping effect which may be due to the increase mapping distance (Fig. S5) where mean TI_{max} values decreased from 0.316 V/m in optimized solutions to 0.305 V/m when mapped (−3.54 %, $p = 3.20 \times 10^{-7}$, |Δ| = 3.77 %, d = −1.09), and maximum values decreased from 0.510 V/m to 0.495 V/m (−2.89 %, $p = 1.48 \times 10^{-6}$, |Δ| = 3.21 %, r = 0.74). Focality also showed a small but statistically significant reduction from 1.526 to 1.487 (−2.55 %, p = 0.00064, |Δ| = 3.56 %, r = 0.54), indicating modest compromise in spatial selectivity for this deeper target (Fig. 5C). Overall, these findings demonstrate that constraining electrode placements to HD-EEG positions resulted in minimal reductions in field intensity across all targets (1–4 %), with focality preserved for cortical and spherical targets, establishing standard HD-EEG montages as a practical solution for TI stimulation without substantially compromising optimization benefits.

3.3. Individualized versus generalized montages

Next, we examined whether a montage optimized on a personalized model provides meaningful advantages over using a consistent montage found via optimization on a generalized head model (Ernie model). Importantly, all simulations used the individualized head models for field calculation. To avoid self-comparison, the generalized model subject was excluded from these analyses (n = 36). For the left insula, individualized models with mapped electrodes achieved higher field intensities than the generalized model, with mean TI_{max} of 0.321 V/m versus 0.312 V/m (+2.70 %, $p = 6.51 \times 10^{-6}$, |Δ| = 3.00 %, d = 0.94) and maximum values of 0.464 V/m versus 0.450 V/m (+3.31 %, $p = 9.88 \times 10^{-5}$, |Δ| = 4.28 %, d = 0.75). Focality showed no significant difference between approaches 1.412 vs 1.413 (+0.05 %, p = 0.93, |Δ| = 3.21 %, r = 0.026) (Fig. 6A–D). The right hippocampus revealed a comparable field intensity between individualized and generalized models. Mean TI_{max} values were virtually identical 0.305 vs 0.302 V/m (+1.21 %, p = 0.213, |Δ| = 3.79 %, d = 0.26), as well as the maximum values 0.497 vs 0.486 V/m (+2.38 %, p = 0.130, |Δ| = 5.81 %, d = 0.35). Focality showed no significant difference between approaches 1.489 vs 1.488 (+0.07 %, p = 0.98, |Δ| = 5.09 %, r = 0.005), suggesting comparable spatial selectivity for this deep target (Fig. 6C–F). For the spherical target, individualized models showed no advantages in field intensity where mean values 0.345 vs 0.339 V/m (+1.866 %, p = 0.006, |Δ| = 3.12 %, d = 0.50) and max values 0.381 vs 0.372 V/m (+2.42 %, p = 0.006, |Δ| = 3.87 %, d = 0.48). Notably, individualized models achieved substantially better focality compared to the template 1.555 vs 1.420 (+9.29 %, $p = 1.75 \times 10^{-7}$, |Δ| = 9.57 %, r = 0.84), indicating superior spatial selectivity when targeting small regions (Fig. 6B–E). Collectively, these findings indicate that personalized montage optimization provides modest but significant advantages over applying a consistent montage found via optimization on a generic model for the left insula (2–3 % higher intensity) and spherical target 9 % better focality, while the right hippocampus showed comparable performance between approaches, suggesting that individualized montage optimization may be particularly valuable for precise focal targeting but less critical for deep subcortical structures.

3.4. Surface-aligned field components

Given the importance of field orientation relative to cortical geometry [15,58,59], we assessed the impact of mapping and generalization described before (sections 3.3 and 3.4) on the normal component of TI_{max} (TI_{normal}) for cortical targets. Comparing mapped to optimized montages for the left insula, mean TI_{normal} decreased from 0.226 V/m to 0.216 V/m (-4.24 %, $p = 1.10 \times 10^{-8}$, |Δ| = 4.37 %, d = −1.28), with maximum values showing similar reductions from 0.402 V/m to 0.394 V/m (−1.86 %, p = 0.024, |Δ| = 4.02 %, d = −0.42). Normal focality remained statistically unchanged 2.265 vs 2.244 (−0.91 %, p = 0.117, |Δ| = 2.50 %, r = 0.26), suggesting preserved directional selectivity despite electrode constraints (Fig. 7A). For the spherical target (using the max optimization that maximized TI_{normal}), comparable sensitivity of the normal component to electrode mapping was observed, with mean values decreasing from 0.201 V/m to 0.192 V/m (−4.66 %, $p = 1.66 \times 10^{-5}$, |Δ| = 5.60 %, Cohen's d = −0.88) and maximum values from 0.351 V/m to 0.343 V/m (Δ = −0.0073 V/m, −2.09 %, p = 0.006, |Δ| = 3.27 %, d = 0.46). Normal focality showed no reduction for the mapped condition 2.025 vs 1.983 (−2.05 %, p = 0.06, |Δ| = 5.06 %, Cohen's d = −0.31) (Fig. 7C). When comparing individualized mapped montages to the montage suggested by a generalized model, the left insula showed no difference in mean TI_{normal} 0.217 V/m for mapped vs 0.216 V/m for Ernie (+0.27 % p = 0.647, |Δ| = 2.24 %, d = 0.09), though individualized models achieved higher maximum values 0.396 vs 0.382 V/m (+3.52 %, p = 0.002, |Δ| = 5.30 %, d = 0.55) at the cost of reduced focality 2.241 vs 2.342, (−4.31 %, p = 0.003, |Δ| = 5.30 %, r = 0.56) (Fig. 7B). The spherical target demonstrated more pronounced differences, with individualized models showing lower mean TI_{normal} 0.191 vs 0.220 V/m (−13.08 %, p = 0.0002, |Δ| = 15.50 %, r = 0.65) but higher maximum values 0.344 vs 0.332 V/m (+3.74 %, p = 0.0002, |Δ| = 4.78 %, r = 0.67) and substantially reduced focality 1.971 vs 2.293 (−14.01 %, p = 0.0003, |Δ| = 17.01 %, r = 0.63) (Fig. 7D). Taken together, these findings indicate that surface-aligned normal field components showed similar sensitivity to electrode mapping as TI_{max} metrics (2–5 % reductions), with preserved focality, while comparisons between individualized and generalized models revealed complex trade-offs between intensity and focality.

3.5. Determinants of inter-individual variability

To identify anatomical and demographic factors underlying inter-individual variability in TI field exposure, we analyzed data from the optimized electrode montages across all targets. Initial correlation analysis revealed strong within-tissue correlations (Fig. S4), with bone thickness and volume showing correlations exceeding r = 0.9, and similar patterns for CSF and skin measures. Based on this multicollinearity assessment, we selected volume measures over thickness measures for subsequent analyses as described in section 2.6.4. To quantify the overall variance explained by anatomical factors, we performed MLR analyses with age, CSF volume, bone volume, and skin volume as predictors of mean TI_{max} in the three ROIs. For the left insula, these anatomical features collectively explained 46.9 % of the variance in field intensity ($R^2 = 0.469$, adjusted $R^2 = 0.400$, F = 6.833, $p = 4.59 \times 10^{-4}$), indicating substantial predictive power. Individual predictors showed that bone volume (β = −0.000430, p = 0.0024) and skin volume (β = −0.000600, p = 0.0248) were significant predictors of field intensity, while CSF volume (β = −0.000113, p = 0.5227) and age (β = −0.000134, p = 0.8315) showed no significant associations. The right hippocampus model showed comparable explanatory power, with anatomical features accounting for 41.1 % of variance ($R^2 = 0.411$, adjusted $R^2 = 0.335$, F = 5.411, $p = 2.01 \times 10^{-3}$). Similarly, bone volume (β = −0.000314, p = 0.0166) and skin volume (β = −0.000574,

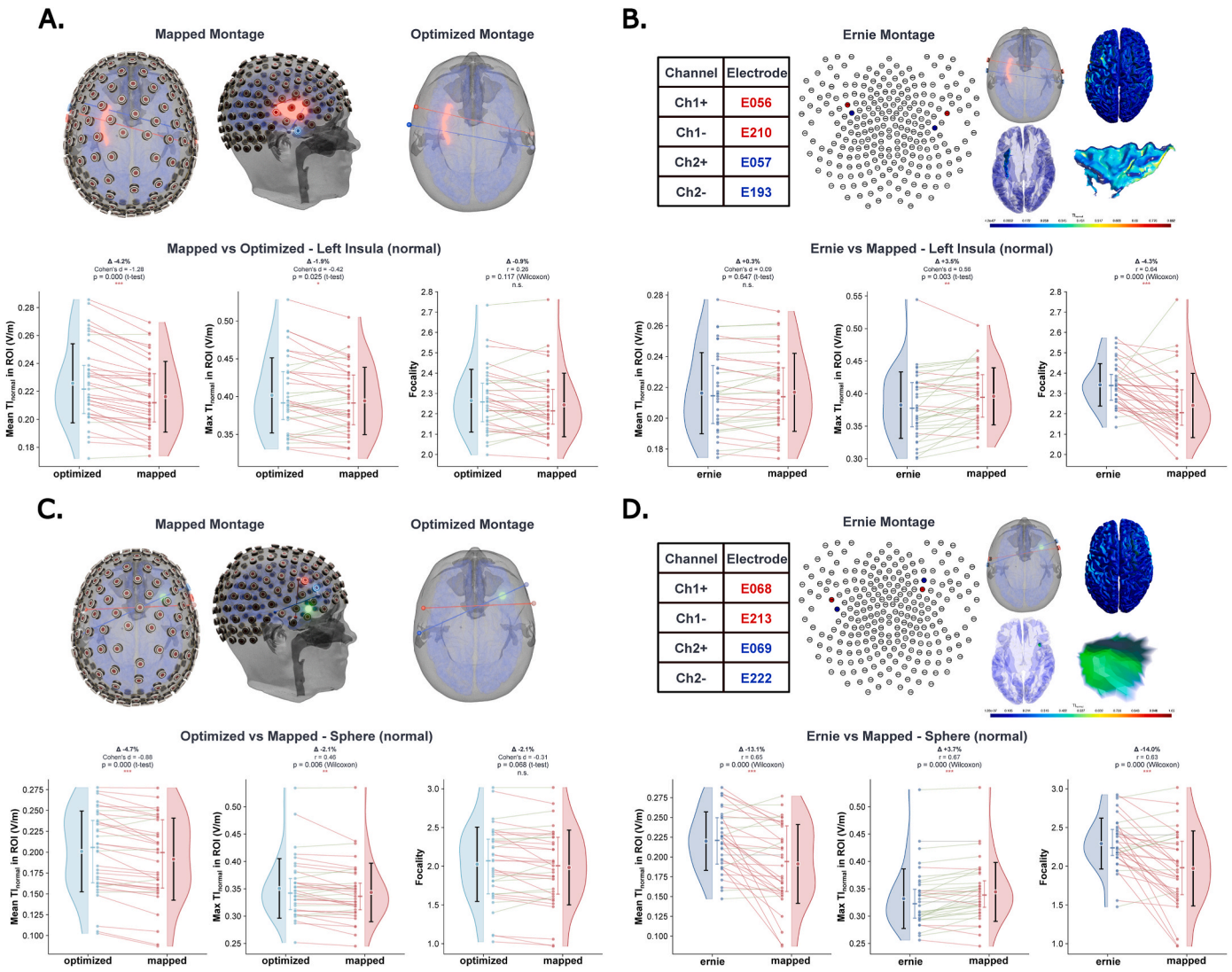

Fig. 7. *Surface-aligned normal component (TI_{normal}) analysis for cortical and spherical targets.* ***A.*** *Left insula comparison between optimized and mapped electrode montages for TI_{normal} field component (optimization goal: maximize mean TI_{normal}). Mean values decreased from 0.226 to 0.*216 V/m *(Δ = -4.24 %, p = 1.10×10^{-8}), while focality remained preserved (p = 0.117).* ***B.*** *Left insula comparison between individualized mapped montages and generalized model (Ernie) for TI_{normal} (optimization goal: maximize mean TI_{normal}). No significant difference in mean values (0.*216 V/m *for both,* p = 0.647*), though individualized models achieved higher maximum values (+3.52 %,* p = 0.002*) with reduced focality (-4.31 %,* p = 0.0002*).* ***C.*** *Spherical target comparison between optimized and mapped montages for TI_{normal} (optimization goal: maximize maximum TI_{normal}). Mean values decreased from 0.201 to 0.*192 V/m *(Δ = -4.66 %, p = 1.66×10^{-5}), with non-significant focality reduction* (p = 0.06)*.* ***D.*** *Spherical target comparison between individualized and generalized models for TI_{normal} (optimization goal: maximize maximum TI_{normal}). Individualized models showed lower mean values (0.191 vs 0.*220 V/m*, -13.08 %, p = 0.0002) but higher maximum values (+3.74 %, p = 0.0002) with substantially reduced focality (-14.01 %, p = 0.0003). Colored lines connect paired observations from the same participant (green for increase, red for decrease, gray for no change), illustrating individual response to different montage conditions. Half violin plots show density distributions. Colored circles represent group means with black vertical lines indicating ±SD while rectangles with vertical lines indicate inter-quartile range (IQR). Statistical comparisons were performed using paired t-test or Wilcoxon signed-rank test with significance denoted as: p < 0.001, p < 0.01, p < 0.05, n.s. = not significant. Effect size (Cohen's d/r) and percentage change are displayed above each comparison. TI_{max} are expressed as V/m.*

p = 0.0245) emerged as significant predictors. CSF volume showed a marginally significant association (β = −0.000311, p = 0.0720), approaching the significance threshold, while age remained non-significant (β = 0.000358, p = 0.5515). For the spherical target (centered at MNI coordinates 36.10, 14.14, 0.33, r = 5 mm) anatomical features explained 31 % of the variance in field intensity (R^2 = 0.309, adjusted R^2 = 0.221, F = 3.4773, p = 1.85×10^{-2}). While none of the individual predictor reached significance, the trend remained consistent with the other ROIS where bone volume (β = −0.000317, p = 0.0631), skin volume (β = −0.000558, p = 0.0925) were significant predictors, and CSF volume (β = −0.00038, p = 0.0956) showed. while age (β = −0.000146, p = 0.854) showed no significant association. Collectively, the model explained 31–47 % of inter-individual variability in mean TI_{max} across all three targets. Bone, skin, and CSF volumes emerged as significant predictors, while age showed no significant associations.

4. Discussion

4.1. TI-Toolbox: strengths and the gap it closes

TI-Toolbox unifies the end-to-end TI workflow—from DICOM pre-processing and head-model generation through montage optimization, field simulation, analysis, and visualization —under a single, containerized framework with both GUI and CLI access. The platform lowers technical barriers, promotes standardized outputs and reports, and enables reproducible, cohort-level studies. Beyond orchestration, it adds TI-specific capabilities: electrode mapping from free solutions to a variety of EEG nets (Table S5), support for multiple optimization

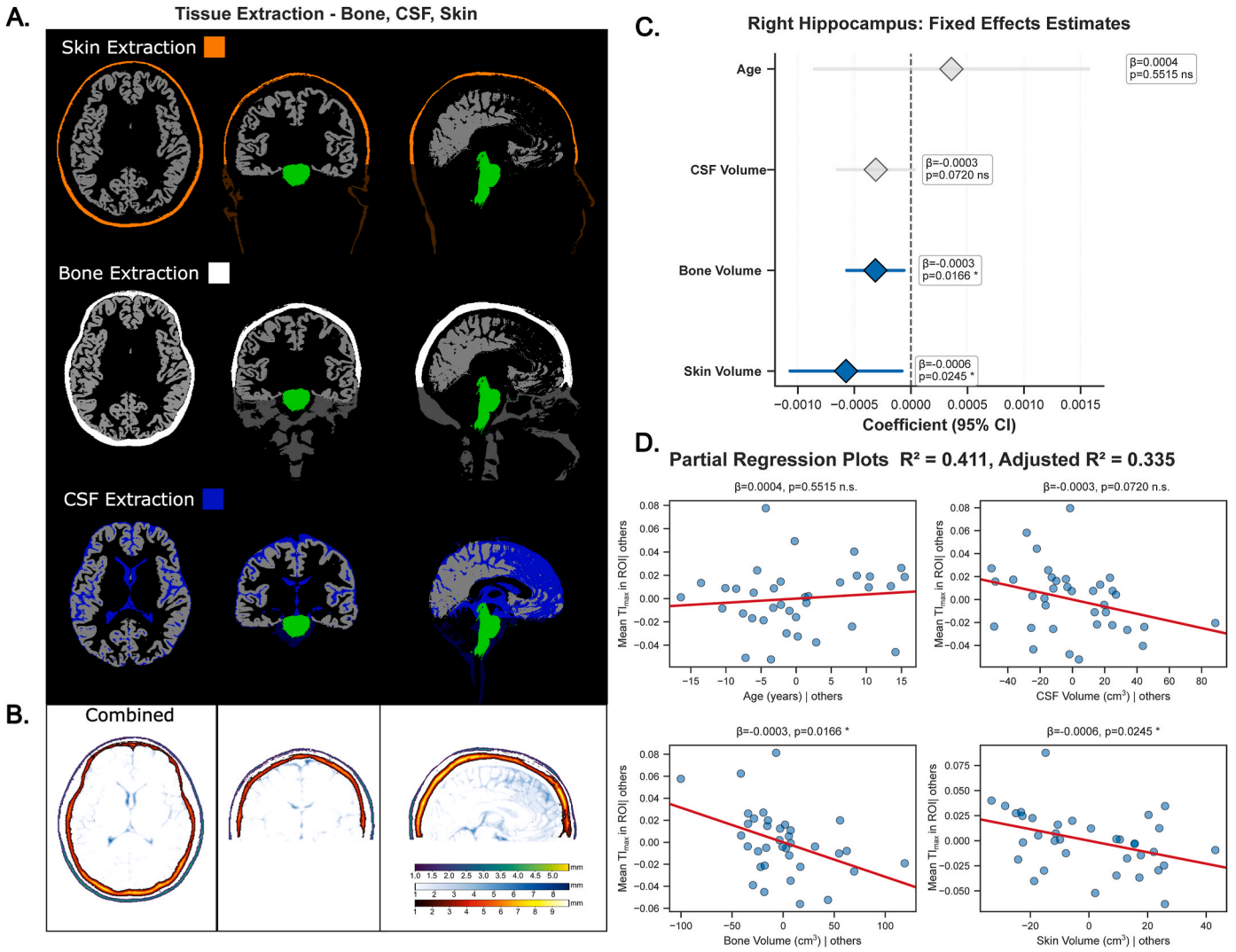

Fig. 8. Anatomical determinants of inter-individual variability in TI field exposure. **A.** *Representative tissue segmentation from a single participant displayed in axial, coronal, and sagittal views. Skin (orange), gray matter (gray) and cortical bone structures (white, including compact and spongy bone layers), cerebrospinal fluid (CSF) highlighting subarachnoid and ventricular CSF distributions (dark blue).* **B.** *Visualization of skin, skull and CSF mean thickness mapping, with color gradient indicating thickness variations (scale: X-Y mm).* **C.** *Multiple linear regression coefficient forest plot for right hippocampus showing standardized coefficients and 95 % confidence intervals. Bone volume (β = -0.0003, p = 0.0166) and skin volume (β = -0.0006, p = 0.0245) emerged as significant predictors, CSF volume approached significance (β = -0.0003, p = 0.0720), while age showed no association (β = -0.0004, p = 0.5515).* **D.** *Partial regression plots demonstrating predictor-outcome relationships for right hippocampus TI_{max} field intensity while controlling for other variables in the model. Individual data points represent participants (n = 36) with regression lines and significance indicators (*p < 0.05, n.s. = not significant).*

approaches, computation of both TI_{max} and gray matter surface-aligned TI_{normal}, and multi-polar simulations. Every module comes with sensible defaults to allow clinical researchers without extensive computational background to build models, run optimizations and visualize results within a few mouse clicks.

4.2. Related software and the SimNIBS foundation

We chose to build TI-Toolbox as an integrated wrapper around SimNIBS [60] for several compelling reasons. First, SimNIBS provides a Python-based interface that enables programmatic access to all core functionalities, facilitating easy integration. This allowed us to extend its capabilities while maintaining compatibility with its core functionalities. Second, SimNIBS has been validated through peer-reviewed studies comparing simulated fields with intracranial recordings [17,61]. Lastly, SimNIBS benefits from an active community of developers and users who continuously contribute improvements, bug fixes, and methodological advances.

However, other solutions that allow for computation of TI in silico exist, each with distinct capabilities. Dedicated commercial solutions include the TI Planning Tool (IT'IS Foundation) [21,62] and HD-Targets-IFS (Soterix Medical) [22]. The TI Planning tool provides multi-objective optimization, model individualization and have a web-based approach removing local installation requirements while the HD-Targets-IFS has a more limited set of functionalities utilizing the MNI model. Notably, both commercial platforms deliver robust solutions but typically require licensing fees and operate within closed-source environments, potentially limiting reproducibility and adaptation. Moreover, multiphysics solutions such as Sim4Life (ZMT Zurich MedTech AG) [23] and COMSOL can provide TI simulation capabilities. While Sim4Life has been used extensively throughout the TI literature [11,46,63] fewer research groups have chosen to rely on COMSOL for their TI modeling efforts possibility due to increased complexity and lack of integration within the TI research community [24,64].

Aside of commercial solutions, other open-source alternatives that

are not TI specific allow for computation of TI. Among them are COMETS2 and ROAST [25,26], MATLAB based packages initially developed for tES computation and now extend that to TI. However, a MATLAB license and high technical abilities are required which may hinder a wider adoption by the clinical community. More recently, the o^{2}S^{2}PARC platform [65] was introduced which provides a significant contribution to support open-science. Developed as part of the NIH's SPARC program, o^{2}S^{2}PARC is a cloud-based, browser-accessible platform that promotes collaborative, and sustainable computational modeling in neuroscience. For TI, users can construct workflows that integrate multi-physics modeling capabilities for TI optimization [66], with post-processing services including 3D visualizations and custom analytics tools. However, the computational blocks integrated within o^{2}S^{2}PARC which are required for the complete TI workflow are not open-source.

4.3. Case studies: summary and interpretation

Our case studies reveal several important insights for the practical implementation of TI stimulation. While some of our comparisons reached statistical significance, it is crucial to distinguish between statistical and clinical relevance. The cohort-level mean percentage differences were small, ranging from approximately 1–4 %, and in isolation are unlikely to be clinically meaningful as intensity remains far within sub-threshold stimulation regime [67–69]. However, dedicated efforts should investigate the possibility of using TI for neural entrainment where such field variance may be critical [70,71].

The validity of electrode mapping emerged as a particularly encouraging finding for clinical translation. When we mapped unconstrained genetic optimization solutions to standard HD-EEG net positions, the resulting montages preserved both intensity and focality characteristics without substantially impairing optimization benefits (Fig. 5). This preservation of field characteristics suggests that mapping offers a practical route to montage standardization and smoother clinical translation, eliminating the need for specialized neuronavigation devices while maintaining targeting efficacy. The successful mapping validates the use of pre-manufactured HD-EEG nets in clinical settings, potentially reducing both cost and complexity of TI implementation.

Similarly, montages optimized on a generalized head model proved adequate for both cortical and subcortical targets when applied to individual head models, suggesting that initial montage design and optimization can proceed without individual MRI scans. However, in line with previous research, accurate exposure assessment clearly requires individualized models due to the substantial inter-individual variability observed in our cohort [2,30,66,72]. This finding supports a hybrid workflow where generalized models guide initial protocol development, while individualized models enable precise dose determination and safety assessment for clinical applications [19,20]. It is important to note that our analysis assumes quasi-uniform field distributions within ROIs when computing mean values, while in reality the fields exhibit spatial gradients and hotspots that may have differential physiological effects depending on the specific neural circuits engaged [73] (Fig. S7). Furthermore, our analyses revealed that TI_{normal} did not demonstrate superior sensitivity to methodological manipulations compared to TI_{max} when evaluating mapping effects or model individualization.

Finally, analysis of inter-individual variability revealed that tissue composition plays a critical role in determining field exposure patterns. Consistent with previous tES literature [53,74,75], anatomical features of the head substantially influence electric field penetration and distribution. Our multiple linear regression analyses quantified these relationships, demonstrating that anatomical features (age, CSF volume, bone volume, and skin volume) collectively explained 46.9 % of variance in field intensity for the left insula and 41.1 % for the right hippocampus using optimized montages. Bone volume and skin volume emerged as significant predictors for both targets, confirming their consistent role as barriers to electric field penetration. Interestingly, CSF volume showed a marginally significant association ($p = 0.0720$) for the right hippocampus but not for the left insula ($p = 0.5227$), likely reflecting the hippocampus's proximity to the ventricular system where CSF-filled spaces create more pronounced current shunting effects. Age showed no significant association with field intensity in either target, suggesting that anatomical characteristics mediate any age-related effects on field penetration. Importantly, inter-subject variability in TI exposure has been linked to functional outcomes, as demonstrated by Violante et al. (2023) who found that participants' evoked BOLD signal in the hippocampus was inversely correlated to TI field intensity, highlighting the potential clinical relevance of individualized field predictions for understanding treatment response variability [11].

These findings highlight a critical translational opportunity: developing predictive models that estimate key anatomical parameters from readily obtainable clinical measurements. While our study demonstrates that bone volume, skin volume, and CSF volume are primary determinants of TI field exposure, obtaining these metrics requires MRI scanning that may be unavailable in many clinical settings. Future research should investigate whether easily acquired measurements such as head circumference, demographic variables (age, sex, ethnicity), body mass index, could serve as proxy predictors for these volumetric parameters. Machine learning approaches could potentially map these accessible metrics to the anatomical features that govern field penetration, enabling clinicians to approximate individualized exposure estimates without neuroimaging.

4.4. Limitations

Several limitations warrant consideration when interpreting our findings. First, our simulations employed isotropic conductivity values and did not leverage diffusion-derived anisotropy which could influence field exposure. However, there is not enough evidence that an anisotropic approach is necessary for targeting gray matter ROIs [76]. Future research should systematically investigate the impact of incorporating DTI on TI field distributions.

Second, all electromagnetic field calculations relied on the quasi-static approximation, which assumes that propagation and inductive effects are negligible at the frequencies employed in TI stimulation (typically 1–20 kHz carriers) [9]. While this approximation is widely accepted for conventional tES and has been validated for frequencies up to several kilohertz in biological tissues [77], the validity at TI carrier frequencies warrants continued investigation [78].

Third, our electrode mapping approach, while successful in preserving field characteristics, was evaluated using only the inner 185 electrodes of the GSN-HydroCel-256 system (EGI/Philips) [79] (Fig. S9). This high-density array provides smaller inter-electrode spacing compared to traditional EEG nets, which may represent an upper bound for successful mapping resolution. The minimum electrode density required for accurate mapping of optimized TI montages remains unexplored, and future work should systematically evaluate how mapping fidelity degrades with decreasing electrode density, particularly for standard 10-10 or 10–20 with larger inter-electrode distances. However, a secondary analysis revealed that 10:10 systems with significantly sparser electrode coverage may still remain an adequate solution for the mapping functionality while the sparser 10:20 system cannot sustain the field characteristics qualities compared to the freely optimized positions [80] (Fig. S8).

Finally, the tissue analyzer module represents an experimental tool that, while providing consistent measurements of anatomical properties across our cohort, has not been independently validated against ground-truth measurements from high-resolution CT imaging [81] or other specialized segmentation methods [82]. Nevertheless, it serves as an informative tool for researchers performing computational modeling by automatically extracting key anatomical metrics that our results and the broader tES literature consistently identify as primary contributors to inter-individual variability. The automated extraction of tissue metrics

provides researchers with readily available covariates that can explain substantial portions of field variance. This functionality aims to support hypothesis generation and covariate adjustment in group studies rather than provide clinical-grade morphometric assessment.

4.5. Implications and future directions

The development and validation of TI-Toolbox carries several implications for the broader TI research community. As an open-source platform, the TI-Toolbox provides an opportunity for collaborative advancement of TI methodologies. We encourage researchers to not only utilize the platform but also to contribute improvements and share workflows in its dedicated GitHub Discussion page [83]. TI-Toolbox follows BIDS input/output best practices. Therefore, project directories and their data can benefit from natural integration with existing BIDS-APPS [84] like fMRIPrep and MRIQC [85] which can ease data processing and sharing [49,85]. We encourage users and contributors to utilize our dedicated Discussion and Issue pages to discuss contribution opportunities and report undesired behavior. This community-driven approach will be essential for establishing standardized protocols and accelerating the development of interoperable tools across different research groups and clinical centers.

Our findings also inform best practices for clinical implementation of TI stimulation. The evidence suggests that prospective clinical studies should adopt a tiered approach to model complexity. While generalized head models can effectively guide initial montage design and protocol development, individualized models become crucial when relating exposure to electrophysiological and behavioral outcomes [66,67]. This distinction is particularly important for dose-response studies and for understanding inter-individual variability in treatment response [11,86]. The substantial variance in field exposure across individuals, even with identical montages as seen here and in Karimi et al., 2025 [66], underscores the necessity of subject-specific modeling for precision medicine applications.

Regarding field assessment metrics, the TI-Toolbox support reporting strategies that capture multiple aspects of TI stimulation. Because the mechanisms underlying TI stimulation remains unclear, we recommend that researchers report both TI_{max} and TI_{normal}, as these metrics provide complementary information about field intensity and directionality though their appropriateness is to be determined. While TI_{max} remains the primary metric for overall exposure assessment, TI_{normal} may prove particularly relevant for understanding interactions with columnar cortical organization [87,88]. Future work should continue to develop concurrent stimulation-recording and closed-loop paradigms to elucidate the online physiological effects of TI in humans and emphasize the relevant properties that researchers should optimize for [14,66,89]. The field will also benefit from direct measurements of fields via intracranial systems that can be used to test the accuracy of in silico models and better inform safety recommendations [5,17].

Furthermore, our secondary analysis revealed a nuanced picture that can inform future studies (Fig. S7). Mean-based optimization promoted a more homogeneous field distribution across the target region, potentially engaging a larger proportion of the neural population while avoiding hotspots that may dominate max-based optimization strategies (Fig. S7C). However, max-based optimization reached a higher peak in both larger and small cortical regions (Fig. S7A and B). Based on our analysis, we recommend the usage of mean-based optimization for larger ROIs to promote field homogeneity while smaller targets or subregions may benefit from a max-based optimization. Researchers should formally define their stimulation objectives and ROIs and apply the appropriate optimization goal when deriving montages.

Finally, our experience with optimization algorithms provides guidance for practical implementation. The flex-search algorithm achieves field intensities comparable to, if not better than, existing optimization algorithms reported in the literature [90]. The multi-start strategy with three independent runs effectively minimizes the optimization function value and improves targeting, as demonstrated for the spherical ROI where it yielded a 4.18 % improvement. However, this modest gain must be weighed against the tripled computational cost, suggesting that single runs may suffice for many applications (Fig. S1).

Validation of flex-search results using a local search, where we evaluated four candidate electrode positions around each optimized electrode location, agreed with the flex-search suggestion, confirming the robustness of the genetic algorithm and mapping approach (Table S2). Furthermore, sweeping through the current ratios did not improve the flex-search solution which assumed a 1:1 current ratio (Table S2). Future research should systematically investigate the impact of including current ratio as a decision variable vs a fixed 1:1 on quality of solution and computational cost. The optimization approaches offered in the TI-Toolbox are complementary to one another. While the flex-search is our recommended method due to the short runtime and its theoretical ability to find global optimum with appropriate tuning of hyper-parameters, it provides no control over electrode placements. Thus, the ex-search can become useful to researchers and clinicians wishing to control the positions available during the optimization search (Fig. 2B upper). This can become increasingly useful when real-world limitations are accounted for like bad impedances in the occipital and lateral regions [91] or surgical intracranial implants.

The focality optimization objective proved more nuanced and context-dependent, requiring careful consideration of thresholding strategies. Our analysis revealed that dynamic thresholding dramatically affects results - 50 % relative thresholds increased focality by 75 % compared to fixed thresholds, while 80 % thresholds decreased it by 36.6 %. This suggests that optimal threshold selection is critical for successful optimization (Fig. S3) [42]. Further research should be conducted into the relationship of the dynamic thresholding and ROI location as it is possible that more superficial ROIs will benefit from high upper bound thresholds while converging successfully on a more focal solution.

4.6. Concluding remarks

Taken together, the case studies support a pragmatic translational pathway: use standardized mapping for clinical usability, leverage a generalized model to prototype montages, and rely on individualized models for exposure quantification and safety assessment. These findings support using mapped montages on standard HD-EEG nets and generalized models for protocol development, with individualized models reserved for precise exposure quantification. TI-Toolbox aims to operationalize a pathway with a reproducible, open, and extensible framework that follows neuroinformatics best practices laying the groundwork for multi-center harmonization and prospective validation for future human studies.

CRediT authorship contribution statement

Ido Haber: Writing – review & editing, Writing – original draft, Visualization, Software, Methodology, Investigation, Formal analysis, Data curation, Conceptualization. **Aksel Jackson:** Writing – review & editing, Writing – original draft, Visualization, Data curation. **Axel Thielscher:** Writing – review & editing, Software, Methodology. **Aviad Hai:** Writing – review & editing. **Giulio Tononi:** Writing – review & editing, Supervision, Funding acquisition, Conceptualization.

Disclosure statement

The authors declare no competing financial or non-financial interests.

Declaration of generative AI use

During the preparation of this work, the author(s) used Cursor for

text and code editing. After using this tool/service, the author(s) reviewed and edited the content as needed and take(s) full responsibility for the content of the published article.

Funding

This project is funded by the Defense Advanced Research Projects Agency (DARPA) under cooperative agreement No. HR00112320033 (to G.T., R.J.D.). The content of the information does not necessarily reflect the position or the policy of the Government, and no official endorsement should be inferred. AT was supported by the Lundbeck Foundation (grant R313-2019-622), the German Research Foundation (project grants TH 1330/6-1 and TH 1330/7-1, part of Research Unit FOR 5429 "MeMoSLAP") and the National Institutes of Health (grant 1RF1MH117428-01A1).

Declaration of competing interest

The authors declare no competing financial or non-financial interests.

Acknowledgements

We wish to thank the staff at University of Wisconsin Brain Imaging Waisman Center and Center for Healthy Minds where the MRI data was collected. We appreciate all study participants for their time and contribution to this work.

Appendix A. Supplementary data

Supplementary data to this article can be found online at https://doi.org/10.1016/j.brs.2025.103016.

Data availability-

Code repository: https://github.com/idossha/TI-Toolbox-
Documentation and tutorials: https://idossha.github.io/TI-Toolbox/

References

[1] Grossman N, et al. Noninvasive deep brain stimulation via temporally interfering electric fields. Cell June 2017;169(6):1029–1041.e16. https://doi.org/10.1016/j.cell.2017.05.024.
[2] Von Conta J, Kasten FH, Ćurčić-Blake B, Aleman A, Thielscher A, Herrmann CS. Interindividual variability of electric fields during transcranial temporal interference stimulation (tTIS). Sci Rep Oct. 2021;11(1):20357. https://doi.org/10.1038/s41598-021-99749-0.
[3] Budde RB, Williams MT, Irazoqui PP. Temporal interference current stimulation in peripheral nerves is not driven by envelope extraction. J Neural Eng Apr. 2023;20(2):026041. https://doi.org/10.1088/1741-2552/acc6f1.
[4] Opančar A, Ondráčková P, Rose DS, Trajlinek J, Đerek V, Głowacki ED. The same biophysical mechanism is involved in both temporal interference and direct kHz stimulation of peripheral nerves. Nat Commun Oct. 2025;16(1):9006. https://doi.org/10.1038/s41467-025-64059-w.
[5] Missey F, et al. Non-invasive temporal interference stimulation of the hippocampus suppresses epileptic biomarkers in patients with epilepsy: biophysical differences between kilohertz and amplitude modulated stimulation. Neurology Dec. 11, 2024. https://doi.org/10.1101/2024.12.05.24303799.
[6] Mirzakhalili E, Barra B, Capogrosso M, Lempka SF. Biophysics of temporal interference stimulation. Cell Syst Dec. 2020;11(6):557–572.e5. https://doi.org/10.1016/j.cels.2020.10.004.
[7] Luff CE, et al. The neuron mixer and its impact on human brain dynamics. Cell Rep June 2024;43(6):114274. https://doi.org/10.1016/j.celrep.2024.114274.
[8] Mansourinezhad P, Mestrom RMC, Klooster DCW, Sprengers M, Boon PAJM, Paulides MM. Systematic review of experimental studies in humans on transcranial temporal interference stimulation. J Neural Eng Oct. 2025;22(5):051001. https://doi.org/10.1088/1741-2552/ae0524.
[9] I. Demchenko et al., "Human applications of transcranial temporal interference stimulation: a systematic review".
[10] Soroushi H, Abbasi S, Du Y, Ning N, Lei Y. Temporal interference stimulation: mechanisms, optimization, validation, and clinical prospects—A comprehensive review. WIREs Comput Stat Sept. 2025;17(3):e70031. https://doi.org/10.1002/wics.70031.
[11] Violante IR, et al. Non-invasive temporal interference electrical stimulation of the human hippocampus. Nat Neurosci Nov. 2023;26(11):1994–2004. https://doi.org/10.1038/s41593-023-01456-8.
[12] Ma R, et al. High gamma and beta temporal interference stimulation in the human motor cortex improves motor functions. Front Neurosci Jan. 2022;15:800436. https://doi.org/10.3389/fnins.2021.800436.
[13] Zhang Y, et al. Temporal interference stimulation targeting right frontoparietal areas enhances working memory in healthy individuals. Front Hum Neurosci Oct. 2022;16:918470. https://doi.org/10.3389/fnhum.2022.918470.
[14] E. L. Schaeffer et al., "Enhancement of sleep slow wave activity using transcranial electrical stimulation with temporal interference".
[15] Meng W, Zhang C, Wu C, Huo X, Zhang G. Direction of TIS envelope electric field: perpendicular to the longitudinal axis of the hippocampus. J Neurosci Methods June 2025;418:110416. https://doi.org/10.1016/j.jneumeth.2025.110416.
[16] Laakso I, Mikkonen M, Koyama S, Hirata A, Tanaka S. Can electric fields explain inter-individual variability in transcranial direct current stimulation of the motor cortex? Sci Rep Jan. 2019;9(1):626. https://doi.org/10.1038/s41598-018-37226-x.
[17] Liu R, et al. Temporal interference stimulation targets deep primate brain. Neuroimage May 2024;291:120581. https://doi.org/10.1016/j.neuroimage.2024.120581.
[18] Renton AI, et al. Neurodesk: an accessible, flexible and portable data analysis environment for reproducible neuroimaging. Nat Methods May 2024;21(5):804–8. https://doi.org/10.1038/s41592-023-02145-x.
[19] Cassarà AM, et al. Recommendations for the safe application of temporal interference stimulation in the human brain part I: principles of electrical neuromodulation and adverse effects. Bioelectromagnetics Feb. 2025;46(2):e22542. https://doi.org/10.1002/bem.22542.
[20] Cassarà AM, et al. Recommendations for the safe application of temporal interference stimulation in the human brain part II: biophysics, dosimetry, and safety recommendations. Bioelectromagnetics Jan. 2025;46(1):e22536. https://doi.org/10.1002/bem.22536.
[21] TI plan - it'IS [Online]. Available, https://tip.science/. [Accessed 10 August 2025].
[22] Neurotargeting software HD-Targets-IFS – Soterix medical [Online]. Available, https://soterixmedical.com/research/software/hd-targets-ifs. [Accessed 10 August 2025].
[23] Neufeld E, Szczerba D, Chavannes N, Kuster N. A novel medical image data-based multi-physics simulation platform for computational life sciences. Interface Focus Apr. 2013;3(2):20120058. https://doi.org/10.1098/rsfs.2012.0058.
[24] Seibt_2019-comsol.".
[25] Lee C, Jung Y-J, Lee SJ, Im C-H. COMETS2: an advanced MATLAB toolbox for the numerical analysis of electric fields generated by transcranial direct current stimulation. J Neurosci Methods Feb. 2017;277:56–62. https://doi.org/10.1016/j.jneumeth.2016.12.008.
[26] Huang Y, Datta A, Bikson M, Parra LC. ROAST: an open-source, fully-automated, realistic volumetric-approach-based simulator for TES. In: 2018 40th annual international conference of the IEEE engineering in medicine and biology society (EMBC). Honolulu, HI: IEEE; July 2018. p. 3072–5. https://doi.org/10.1109/EMBC.2018.8513086.
[27] Thielscher A, Antunes A, Saturnino GB. Field modeling for transcranial magnetic stimulation: a useful tool to understand the physiological effects of TMS?. In: 2015 37th annual international conference of the IEEE engineering in medicine and biology society (EMBC). Milan: IEEE; Aug. 2015. p. 222–5. https://doi.org/10.1109/EMBC.2015.7318340.
[28] Lee S, Lee C, Park J, Im C-H. Individually customized transcranial temporal interference stimulation for focused modulation of deep brain structures: a simulation study with different head models. Sci Rep July 2020;10(1):11730. https://doi.org/10.1038/s41598-020-68660-5.
[29] Chan W, Wang X, Qiu B, Wang Y. Impact of electrode drift in multi-electrode temporal interference stimulation. In: 2025 5th international conference on neural networks, information and communication engineering (NNICE); Jan. 2025. p. 782–6. https://doi.org/10.1109/NNICE64954.2025.11064315.
[30] Brahma T, Guillen A, Moreno J, Datta A, Huang Y. On the need of individually optimizing temporal interference stimulation of human brains due to inter-individual variability. Biophysics Jan. 17, 2025. https://doi.org/10.1101/2025.01.13.632831.
[31] Geuzaine C, Remacle J-F. Gmsh: a 3-D finite element mesh generator with built-in pre- and post-processing facilities. Int J Numer Methods Eng 2009;79(11):1309–31. https://doi.org/10.1002/nme.2579.
[32] Fischl B. FreeSurfer. Neuroimage Aug. 2012;62(2):774–81. https://doi.org/10.1016/j.neuroimage.2012.01.021.
[33] Willman J. Modern PyQt: create GUI applications for project management, computer vision, and data analysis. Berkeley, CA: Apress; 2021. https://doi.org/10.1007/978-1-4842-6603-8.
[34] PyQt - python wiki [Online]. Available, https://wiki.python.org/moin/PyQt. [Accessed 10 August 2025].
[35] Docker: accelerated container application development [Online]. Available, https://www.docker.com/. [Accessed 10 August 2025].
[36] Boettiger C. An introduction to docker for reproducible research. ACM SIGOPS - Oper Syst Rev Jan. 2015;49(1):71–9. https://doi.org/10.1145/2723872.2723882.
[37] I. Haber, "Temporal interference toolbox," Temporal Interference Toolbox. Accessed: August. 10, 2025. [Online]. Available: https://idossha.github.io/TI-Toolbox/.

[38] Mazziotta J, et al. A probabilistic atlas and reference system for the human brain: International consortium for brain mapping (ICBM). Philos Trans R Soc Lond B Biol Sci Aug. 2001;356(1412):1293–322. https://doi.org/10.1098/rstb.2001.0915.

[39] Li X, Morgan PS, Ashburner J, Smith J, Rorden C. The first step for neuroimaging data analysis: DICOM to NIfTI conversion. J Neurosci Methods May 2016;264:47–56. https://doi.org/10.1016/j.jneumeth.2016.03.001.

[40] Tange O. Gnu parallel 2018. Zenodo; 2018. https://doi.org/10.5281/ZENODO.1146014.

[41] Puonti O, Van Leemput K, Saturnino GB, Siebner HR, Madsen KH, Thielscher A. Accurate and robust whole-head segmentation from magnetic resonance images for individualized head modeling. Neuroimage Oct. 2020;219:117044. https://doi.org/10.1016/j.neuroimage.2020.117044.

[42] Weise K, Madsen KH, Worbs T, Knösche TR, Korshøj A, Thielscher A. A leadfield-free optimization framework for transcranially applied electric currents. Neuroscience Dec. 20, 2024. https://doi.org/10.1101/2024.12.18.629095.

[43] Alexander B, et al. Desikan-killiany-tourville atlas compatible version of M-CRIB neonatal parcellated whole brain atlas: the M-CRIB 2.0. Front Neurosci Feb. 2019;13:34. https://doi.org/10.3389/fnins.2019.00034.

[44] Destrieux C, Fischl B, Dale A, Halgren E. Automatic parcellation of human cortical gyri and sulci using standard anatomical nomenclature. Neuroimage Oct. 2010;53(1):1–15. https://doi.org/10.1016/j.neuroimage.2010.06.010.

[45] Glasser MF, et al. A multi-modal parcellation of human cerebral cortex. Nature Aug. 2016;536(7615):171–8. https://doi.org/10.1038/nature18933.

[46] Botzanowski B, et al. Focal control of non-invasive deep brain stimulation using multipolar temporal interference. Bioelectron Med Mar. 2025;11(1):7. https://doi.org/10.1186/s42234-025-00169-6.

[47] Blender/blender: official mirror of blender [Online]. Available, https://github.com/blender/blender. [Accessed 20 November 2025].

[48] Gorgolewski KJ, et al. The brain imaging data structure, a format for organizing and describing outputs of neuroimaging experiments. Sci Data June 2016;3(1):160044. https://doi.org/10.1038/sdata.2016.44.

[49] Esteban O, et al. fMRIPrep: a robust preprocessing pipeline for functional MRI. Nat Methods Jan. 2019;16(1):111–6. https://doi.org/10.1038/s41592-018-0235-4.

[50] Build cross-platform desktop apps with JavaScript, HTML, and CSS | electron [Online]. Available, https://electronjs.org/. [Accessed 20 November 2025].

[51] Home," GitHub. Accessed: August. 10, 2025. [Online]. Available: https://github.com/tmux/tmux/wiki/Home.

[52] Differential_evolution — SciPy v1.16.2 manual [Online]. Available: https://docs.scipy.org/doc/scipy/reference/generated/scipy.optimize.differential_evolution.html. [Accessed 24 November 2025].

[53] Opitz A, Paulus W, Will S, Antunes A, Thielscher A. Determinants of the electric field during transcranial direct current stimulation. Neuroimage Apr. 2015;109:140–50. https://doi.org/10.1016/j.neuroimage.2015.01.033.

[54] Saturnino GB, Antunes A, Thielscher A. On the importance of electrode parameters for shaping electric field patterns generated by tDCS. Neuroimage Oct. 2015;120:25–35. https://doi.org/10.1016/j.neuroimage.2015.06.067.

[55] Wagner TA, Zahn M, Grodzinsky AJ, Pascual-Leone A. Three-dimensional head model simulation of transcranial magnetic stimulation. IEEE Trans Biomed Eng Sept. 2004;51(9):1586–98. https://doi.org/10.1109/TBME.2004.827925.

[56] Benjamini Y, Hochberg Y. Controlling the false discovery rate: a practical and powerful approach to multiple testing. J R Stat Soc Ser B Methodol 1995;57(1):289–300. https://doi.org/10.1111/j.2517-6161.1995.tb02031.x.

[57] Brett M, et al. *Nipy/nibabel*: 5.3.1. Zenodo; Oct. 15, 2024. https://doi.org/10.5281/zenodo.13936989.

[58] Kabakov AY, Muller PA, Pascual-Leone A, Jensen FE, Rotenberg A. Contribution of axonal orientation to pathway-dependent modulation of excitatory transmission by direct current stimulation in isolated rat hippocampus. J Neurophysiol Apr. 2012;107(7):1881–9. https://doi.org/10.1152/jn.00715.2011.

[59] Howell B, McIntyre CC. Feasibility of interferential and pulsed transcranial electrical stimulation for neuromodulation at the human scale. Neuromodulation Technol Neural Interface July 2021;24(5):843–53. https://doi.org/10.1111/ner.13137.

[60] Saturnino GB, Puonti O, Nielsen JD, Antonenko D, Madsen KH, Thielscher A. SimNIBS 2.1: a comprehensive pipeline for individualized electric field modelling for transcranial brain stimulation. In: Makarov S, Horner M, Noetscher G, editors. Brain and human body modeling. Cham: Springer International Publishing; 2019. p. 3–25. https://doi.org/10.1007/978-3-030-21293-3_1.

[61] Wang M, et al. In vivo measurements of electric fields during cranial electrical stimulation in the human brain. Front Hum Neurosci Feb. 2022;16:829745. https://doi.org/10.3389/fnhum.2022.829745.

[62] Neufeld E, Maiz O, Kaiser D, Lloyd B, Farcito S. ID# 1906835 planning tool for personalized temporal interference stimulation optimization. Neuromodulation Technol Neural Interface Oct. 2025;28(7):S171. https://doi.org/10.1016/j.neurom.2025.08.324. Supplement.

[63] Wessel MJ, et al. Noninvasive theta-burst stimulation of the human striatum enhances striatal activity and motor skill learning. Nat Neurosci Nov. 2023;26(11):2005–16. https://doi.org/10.1038/s41593-023-01457-7.

[64] Esmaeilpour Z, Kronberg G, Reato D, Parra LC, Bikson M. Temporal interference stimulation targets deep brain regions by modulating neural oscillations. Brain Stimulat Jan. 2021;14(1):55–65. https://doi.org/10.1016/j.brs.2020.11.007.

[65] M. Guidon et al., "Shaping a collaborative, sustainable, accessible, and reproducible future for computational modeling".

[66] Karimi F, et al. Precision non-invasive brain stimulation: an *In silico* pipeline for personalized control of brain dynamics. J Neural Eng Apr. 2025;22(2):026061. https://doi.org/10.1088/1741-2552/adb88f.

[67] Liu A, et al. Immediate neurophysiological effects of transcranial electrical stimulation. Nat Commun Nov. 2018;9(1):5092. https://doi.org/10.1038/s41467-018-07233-7.

[68] Francis JT, Gluckman BJ, Schiff SJ. Sensitivity of neurons to weak electric fields. J Neurosci Aug. 2003;23(19):7255–61. https://doi.org/10.1523/JNEUROSCI.23-19-07255.2003.

[69] Reato D, Rahman A, Bikson M, Parra LC. Low-intensity electrical stimulation affects network dynamics by modulating population rate and spike timing. J Neurosci Nov. 2010;30(45):15067–79. https://doi.org/10.1523/JNEUROSCI.2059-10.2010.

[70] Vieira PG, Krause MR, Pack CC. Temporal interference stimulation disrupts spike timing in the primate brain. Nat Commun May 2024;15(1):4558. https://doi.org/10.1038/s41467-024-48962-2.

[71] Beliaeva V, Savvateev I, Zerbi V, Polania R. Toward integrative approaches to study the causal role of neural oscillations via transcranial electrical stimulation. Nat Commun Apr. 2021;12(1):2243. https://doi.org/10.1038/s41467-021-22468-7.

[72] Yatsuda K, Yu W, Gomez-Tames J. Population-level insights into temporal interference for focused deep brain neuromodulation. Front Hum Neurosci Apr. 2024;18:1308549. https://doi.org/10.3389/fnhum.2024.1308549.

[73] Bikson M, Dmochowski J, Rahman A. The 'Quasi-Uniform' assumption in animal and computational models of non-invasive electrical stimulation. Brain Stimulat July 2013;6(4):704–5. https://doi.org/10.1016/j.brs.2012.11.005.

[74] Antonenko D, Grittner U, Saturnino G, Nierhaus T, Thielscher A, Flöel A. Inter-individual and age-dependent variability in simulated electric fields induced by conventional transcranial electrical stimulation. Neuroimage Jan. 2021;224:117413. https://doi.org/10.1016/j.neuroimage.2020.117413.

[75] Laakso I, Tanaka S, Koyama S, De Santis V, Hirata A. Inter-subject variability in electric fields of motor cortical tDCS. Brain Stimulat Sept. 2015;8(5):906–13. https://doi.org/10.1016/j.brs.2015.05.002.

[76] Mosayebi-Samani M, Cunha T, Eroğlu HH, Siebner HR, Nitsche MA, Thielscher A. The effect of brain tissue anisotropy on the electric field caused by transcranial electric stimulation: sensitivity analysis and magnetic resonance electrical impedance tomography. Imaging Neurosci Feb. 2025;3. https://doi.org/10.1162/imag_a_00481. imag_a_00481.

[77] Miranda PC, Mekonnen A, Salvador R, Basser PJ. Predicting the electric field distribution in the brain for the treatment of glioblastoma. Phys Med Biol Aug. 2014;59(15):4137–47. https://doi.org/10.1088/0031-9155/59/15/4137.

[78] Gaugain G, et al. Quasi-static approximation error of electric field analysis for transcranial current stimulation. J Neural Eng Feb. 2023;20(1):016027. https://doi.org/10.1088/1741-2552/acb14d.

[79] Geodesic sensor nets [Online]. Available: https://www.egi.com/clinical-division/geodesic-sensor-nets. [Accessed 10 August 2025].

[80] Jurcak V, Tsuzuki D, Dan I. 10/20, 10/10, and 10/5 systems revisited: their validity as relative head-surface-based positioning systems. Neuroimage Feb. 2007;34(4):1600–11. https://doi.org/10.1016/j.neuroimage.2006.09.024.

[81] Ku CH, et al. Measurement of skull size on computed tomography images for developing a bone conduction headset suitable for the Korean standard head size. J Audiol Otol Jan. 2020;24(1):17–23. https://doi.org/10.7874/jao.2019.00290.

[82] Calisan M, Talu MF, Pimenov DY, Giasin K. Skull thickness calculation using thermal analysis and finite elements. Appl Sci Nov. 2021;11(21):10483. https://doi.org/10.3390/app112110483.

[83] Multipass, *idossha/TI-Toolbox*. Python Aug. 04, 2025 [Online]. Available: https://github.com/idossha/TI-Toolbox. [Accessed 10 August 2025].

[84] Gorgolewski KJ, et al. BIDS apps: improving ease of use, accessibility, and reproducibility of neuroimaging data analysis methods. PLoS Comput Biol Mar. 2017;13(3):e1005209. https://doi.org/10.1371/journal.pcbi.1005209.

[85] O. Esteban, D. Birman, M. Schaer, O. O. Koyejo, R. A. Poldrack, and K. J. Gorgolewski, "MRIQC: advancing the automatic prediction of image quality in MRI from unseen sites".

[86] Peterchev AV, et al. Fundamentals of transcranial electric and magnetic stimulation dose: definition, selection, and reporting practices. Brain Stimulat Oct. 2012;5(4):435–53. https://doi.org/10.1016/j.brs.2011.10.001.

[87] Radman T, Ramos RL, Brumberg JC, Bikson M. Role of cortical cell type and morphology in subthreshold and suprathreshold uniform electric field stimulation in vitro. Brain Stimulat Oct. 2009;2(4):215–228.e3. https://doi.org/10.1016/j.brs.2009.03.007.

[88] Jones EG. Microcolumns in the cerebral cortex. Proc Natl Acad Sci May 2000;97(10):5019–21. https://doi.org/10.1073/pnas.97.10.5019.

[89] Modak P, et al. Temporal interference electrical neurostimulation at 20 Hz beat frequency leads to increased fMRI BOLD activation in orbitofrontal cortex in humans. Brain Stimulat July 2024;17(4):867–75. https://doi.org/10.1016/j.brs.2024.07.014.

[90] Geng C, Li Y, Li L, Zhu X, Hou X, Liu T. Optimized temporal interference stimulation based on convex optimization: a computational study. IEEE Trans Neural Syst Rehabil Eng 2025;33:1400–10. https://doi.org/10.1109/TNSRE.2025.3558306.

[91] Lees T, Ram N, Swingler MM, Gatzke-Kopp LM. The effect of hair type and texture on electroencephalography and event-related potential data quality. Psychophysiology Mar. 2024;61(3):e14499. https://doi.org/10.1111/psyp.14499.